The Astronomical Journal, 156:286 (25pp), 2018 December https://doi.org/10.3847/1538-3881/aaec00
© 2018. The American Astronomical Society. All rights reserved.

The LEECH Exoplanet Imaging Survey: Limits on Planet Occurrence Rates under Conservative Assumptions

Jordan M. Stone[1,22], Andrew J. Skemer[2], Philip M. Hinz[1], Mariangela Bonavita[3], Kaitlin M. Kratter[1], Anne-Lise Maire[4], Denis Defrere[5], Vanessa P. Bailey[6], Eckhart Spalding[1], Jarron M. Leisenring[1], S. Desidera[7], M. Bonnefoy[8], Beth Biller[3,9], Charles E. Woodward[10], Th. Henning[4], Michael F. Skrutskie[11], J. A. Eisner[1], Justin R. Crepp[12], Jennifer Patience[13], Gerd Weigelt[14], Robert J. De Rosa[15], Joshua Schlieder[4,16], Wolfgang Brandner[4], Dániel Apai[1,4,17], Kate Su[1], Steve Ertel[1], Kimberly Ward-Duong[18], Katie M. Morzinski[1], Dieter Schertl[14], Karl-Heinz Hofmann[14], Laird M. Close[1], Stefan S. Brems[19], Jonathan J. Fortney[2], Apurva Oza[11,20], Esther Buenzli[21], and Brandon Bass[1]

[1] Steward Observatory, University of Arizona, 933 N. Cherry Ave, Tucson, AZ 85721-0065 USA
[2] Department of Astronomy and Astrophysics, University of California, Santa Cruz, 1156 High Street, Santa Cruz, CA 95064, USA
[3] SUPA, Institute for Astronomy, University of Edinburgh, Royal Observatory, Edinburgh EH9 3HJ, UK
[4] Max Planck Institute for Astronomy, Königstuhl 17, D-69117 Heidelberg, Germany
[5] Space sciences, Technologies & Astrophysics Research (STAR) Institute, University of Liège, Liège, Belgium
[6] Jet Propulsion Laboratory, California Institute of Technology, Pasadena, CA, 91109, USA
[7] INAF Osservatorio Astronomico di Padova, vicolo dell Osservatorio 5, I-35122 Padova, Italy
[8] Université Grenoble Alpes, CNRS, IPAG, F-38000 Grenoble, France
[9] Centre for Exoplanet Science, University of Edinburgh, Edinburgh EH9 3HJ, UK
[10] Minnesota Institute of Astrophysics, University of Minnesota, 116 Church Street, SE, Minneapolis, MN 55455, USA
[11] Department of Astronomy, University of Virginia, Charlottesville, VA 22904, USA
[12] Department of Physics, University of Notre Dame, 225 Niuwland Science Hall, Notre Dame, IN, 46556, USA
[13] School of Earth and Space Exploration, Arizona State University, P.O. Box 871404, Tempe, AZ 85287, USA
[14] Max-Planck-Institut für Radioastronomie, Auf dem Hügel 69, D-53121 Bonn, Germany
[15] Astronomy Department, University of California, Berkeley, CA 94720, USA
[16] Exoplanets and Stellar Astrophysics Laboratory, Code 667, NASA Goddard Space Flight Center, 8800 Greenbelt Road, Greenbelt, MD 20771, USA
[17] Lunar and Planetary Laboratory, The University of Arizona, 1629 E. University Boulevard, Tucson, AZ 85721 USA
[18] Five College Astronomy Department, Amherst College, Amherst, MA 01002, USA
[19] Zentrum für Astronomie der Universität Heidelberg, Landessternwarte, Königstuhl 12, D-69117 Heidelberg, Germany
[20] Physikalisches Institut, Universität Bern, Gesellschaftsstrasse 6, CH-3012 Bern, Switzerland
[21] Institute for Particle Physics and Astrophysics, ETH Zurich, Wolfgang-Pauli-Strasse 27, 8093 Zurich, Switzerland
Received 2018 August 14; revised 2018 October 23; accepted 2018 October 24; published 2018 November 29

Abstract

We present the results of the largest L' (3.8 μm) direct imaging survey for exoplanets to date, the Large Binocular Telescope Interferometer Exozodi Exoplanet Common Hunt (LEECH). We observed 98 stars with spectral types from B to M. Cool planets emit a larger share of their flux in L' compared to shorter wavelengths, affording LEECH an advantage in detecting low-mass, old, and cold-start giant planets. We emphasize proximity over youth in our target selection, probing physical separations smaller than other direct imaging surveys. For FGK stars, LEECH outperforms many previous studies, placing tighter constraints on the hot-start planet occurrence frequency interior to ~20 au. For less luminous, cold-start planets, LEECH provides the best constraints on giant-planet frequency interior to ~20 au around FGK stars. Direct imaging survey results depend sensitively on both the choice of evolutionary model (e.g., hot- or cold-start) and assumptions (explicit or implicit) about the shape of the underlying planet distribution, in particular its radial extent. Artificially low limits on the planet occurrence frequency can be derived when the shape of the planet distribution is assumed to extend to very large separations, well beyond typical protoplanetary dust-disk radii ($\lesssim$50 au), and when hot-start models are used exclusively. We place a conservative upper limit on the planet occurrence frequency using cold-start models and planetary population distributions that do not extend beyond typical protoplanetary dust-disk radii. We find that $\lesssim$90% of FGK systems can host a 7–10 $M_{\rm Jup}$ planet from 5 to 50 au. This limit leaves open the possibility that planets in this range are common.

Key words: planetary systems – planets and satellites: gaseous planets – stars: imaging – techniques: high angular resolution

1. Introduction

Understanding the formation and evolution of planetary systems requires a detailed census of the galactic planet population. Surveys sensitive to planets orbiting at a wide range of semimajor axes about stars with a variety of spectral types and ages are required to measure the planet mass and semimajor axis distributions as a function of host mass, age, metallicity, and environment.

The Doppler spectroscopy and transit photometry techniques have excelled at discovering mature planets on short-period orbits about their field-aged (few Gyr) host stars (e.g., Cumming et al. 2008; Batalha 2014). Microlensing surveys have helped constrain the planet population around typically older low-mass stars (e.g., Gould et al. 2010). The direct imaging technique is sensitive to wide-orbit planets typically around younger stars (e.g., Bowler 2016). In this paper, we report the results of the Large Binocular Telescope Interferometer (LBTI) Exozodi Exoplanet Common Hunt (LEECH;

[22] Hubble Fellow.

Skemer et al. 2014a) direct imaging survey of intermediate-aged stars.

The direct imaging technique of planet detection entails high spatial resolution adaptive optics (AO) assisted observations and sophisticated post-processing techniques to separate starlight from planet light (e.g., Marois et al. 2006; Soummer et al. 2012). Since direct imaging involves collecting photons directly from the planetary photosphere, the atmospheres of any newly discovered planets can be studied in detail—potentially leading to constraints on composition and the formation process (Konopacky et al. 2013; Barman et al. 2015; Skemer et al. 2016; Samland et al. 2017).

Past direct imaging surveys (recently reviewed in Bowler 2016) probed orbits with semimajor axes $\gtrsim$10 au (with peak sensitivity $\gtrsim$100 au) for nearby young stars (with typical distances $\sim$50 pc), filling in some of the parameter space not covered by radial-velocity or transit surveys. Probing these outer regions is important because this is the regime where protoplanetary disks are thought to have enhanced surface density of solids due to the freeze-out of volatiles, adding to the raw material available to build up protoplanetary cores (e.g., Hayashi 1981). Therefore, direct imaging provides access to the semimajor axes where giant planets could form in situ (e.g., Ormel & Klahr 2010; Lambrechts & Johansen 2012).

The results of previous direct imaging surveys are conveniently tabulated in Chauvin et al. (2015) and Galicher et al. (2016). Bowler (2016) provides an overview and summary of previous imaging surveys and synthesizes their results in an analysis that combines data from many studies. The main result is that gas-giant planets on orbits $\gtrsim$100 au are rare. As we shall show, interior to $\sim$100 au, constraints on the planet occurrence frequency are less well established and depend on the assumed shape of the planet population distribution, as well as the initial entropy and luminosity evolution of giant planets. In particular, a cold-start population that does not extend beyond typical protoplanetary dust-disk radii remains poorly constrained.

Younger and more massive planets are easier to detect with direct imaging, because planets—lacking an internal heat source—cool and fade as they radiate their gravitational potential energy. As a result, most direct imaging surveys emphasize youth in their target selection to maximize their sensitivity to low-mass gas-giant planets. Selecting for youth is an absolute necessity for surveys conducted at wavelengths $<$2.5 μm, where planet-to-star contrast is a steep function of the planetary effective temperature (e.g., Liu et al. 2010; Chauvin et al. 2015; Galicher et al. 2016; Tamura 2016). However, the planet-to-star contrast is alleviated at longer wavelengths near the peak of a planet's spectral energy distribution. Furthermore, previous discoveries have shown that near-infrared ($\lambda \lesssim 2.5$ μm) emission is suppressed and thermal–infrared (3–5 μm) emission is enhanced for directly imaged planets compared to more massive brown dwarfs at the same effective temperature, a consequence of low surface gravity (e.g., Chauvin et al. 2005; Barman et al. 2011; Skemer et al. 2011; Marley et al. 2012; Filippazzo et al. 2015). We conducted the LEECH survey in the L' band at 3.8 μm to take advantage of an increased sensitivity to cooler planets, including lower-mass planets, older planets, and planets that are born cold because they accrete their envelopes through a radiatively efficient shock (e.g., Marley et al. 2007). We therefore emphasize proximity over youth in our target selection to probe the smallest orbital distances possible given the constraints of diffraction-limited observing at 3.8 μm with an 8.25 m aperture.

Kasper et al. (2007) were the first to perform an L' direct imaging survey, observing 22 stars with the Very Large Telescope (VLT) before the advent of modern high-contrast post-processing algorithms. Additional L' surveys are summarized in Table 1. Our survey includes many of the same targets as the Heinze et al. (2010b) survey, and we probe deeper and closer in to the host star to search for lower-mass planets on shorter period orbits. In Figure 1, we compare the median and best LEECH contrast curves from LBTI/LMIRCam to the median and best contrast curves from the Rameau et al. (2013) survey, which used NACO at the VLT and delivered the deepest contrasts among all the NACO surveys listed in Table 1. The LEECH survey stands out among earlier direct imaging surveys at L', having the largest target list and best median contrast.

Our L' sensitivity is facilitated by the unique architecture of the LBT observatory and the LBTI instrument. The observatory provides twin deformable secondary mirrors each with 672 actuators that routinely deliver images with $\sim$90% Strehl at 3.8 μm (Bailey et al. 2014). By using the secondary mirror as the adaptive element, the LBTAO system minimizes the number of warm optics in the light path to provide low-background, high-throughput thermal and mid-infrared images. LBTI was designed for thermal and mid-infrared science and includes a cryogenic beam combiner for feeding the light from each side of the LBT into the instrument and onto the detector (Hinz et al. 2016). Observations for the LEECH survey were performed in direct imaging mode with LBTI and are not interferometric.

We describe our target selection in Section 2, where we also derive ages for a subset of A- and B-type stars on our target list. Our observing strategy and data processing pipeline are described in Sections 3 and 4, respectively. We present the results of our survey in Section 5. In Section 6, we perform a statistical analysis of the results. We provide a detailed discussion about how different assumptions can significantly alter inferred limits on wide-orbit planet occurrence rates in Section 7. We then outline the conditions for a conservative estimate.

2. Target Selection

The LEECH survey was designed with two facets: (1) a statistical survey to help better inform our understanding of the wide-orbit giant-planet distribution and (2) characterization of known low-mass systems and directly imaged planets. Objects specifically added to the LEECH target list for characterization include HIP 72567 (HD 130948), HIP 114189 (HR 8799, LEECH reference: Maire et al. 2015), HIP 64792 (GJ 504, LEECH reference: Skemer et al. 2016), and HIP 116805 (κ And).

Although characterization targets meet the selection criteria (described below) for our statistical sample target lists, we leave them out of our statistical analysis. These targets were specifically prioritized for observation under good observing conditions and when adequate time could be committed to reach the necessary sensitivity. Because prioritization enhances our ability to detect planets around stars with known companions, including them in our statistical analysis would bias our results. The HIP 21547 (51 Eri) system provides a good example of our reasoning. This system was on our

Table 1
Summary of L' Surveys

Reference	Instrument	Number of Targets	Spectral Types	Median Distance (pc)	Median Age (Myr)
Kasper et al. (2007)	NACO	22	FGKM	37	10–30
Heinze et al. (2010b)	Clio	54	FGKM	11.2	∼200
Delorme et al. (2012)	NACO	16	M	25.4	12[a]
Rameau et al. (2013)	NACO	59	BAFGKM	40	30
Meshkat et al. (2015)	NACO	13	AF	48	40
Lannier et al. (2016)	NACO	58	M	38	21
LEECH	LBTI	98	BAFGKM	25.5	400

Note.
[a] Delorme et al. (2012) assigned a uniform age of 12 Myr to members of the β Pic moving group, and objects from this group dominate their target list, resulting in a 12 Myr median age. Lannier et al. (2016) assigned an age of 21 Myr to these same targets.

original target list and observed by LEECH before the discovery of a directly imaged planet (Macintosh et al. 2015). As discussed below, we obtained only marginal data sets on this star taken through thin clouds. We did not detect the planet. Since the planet around 51 Eri was not known before we observed the system with LEECH, we do include this object in our statistical analysis. Schlieder et al. (2016) presented a characterization of the NO UMa system using LEECH data; however, this system was not specifically targeted for characterization and is also included in our statistical sample.

2.1. Master Target List for Statistical Survey

We compiled a master target list comprising four sublists for use during the LEECH survey. Each sublist carried a slightly different emphasis, though the guiding principles for each were relative proximity and age $\lesssim$1 Gyr.

Our first sublist emphasizes proximity and F/G/K spectral type. Targets for this FGK sublist were drawn from Heinze et al. (2010a) and Mamajek & Hillenbrand (2008). In total we observed 17 stars from the Heinze/Mamajek sublist. Our second sublist is composed of stars in the Ursa Major moving group selected from King et al. (2003). This sublist provides a set of targets, with spectral types ranging from A to M, that all have the same well-constrained age (414 ± 23 Myr; Jones et al. 2015). We observed 31 stars from the UMa sublist. Our third sublist includes A- and F-type stars that show evidence of a debris disk, drawn from Gáspár et al. (2013). In total, we observed 17 stars from this Dusty-A/F sublist. Finally, our fourth sublist includes B- and A-type field stars with estimated ages $\lesssim$1 Gyr (see Section 2.2). We observed 33 stars from this Field-B/A sublist.

During observing nights, we selected targets from our master list based on (1) the total amount of parallactic angle change accessible in a three-hour block and (2) the position of the target with respect to the wind velocity, which restricts azimuth angles accessible for good AO performance. Stars were also prioritized by our best guess for the probability of hosting a wide-orbit gas-giant planet based on planet frequency correlations with host-star properties deduced from radial-velocity surveys (e.g., mass and metallicity; Crepp & Johnson 2011), although observing conditions at the telescope typically drove nightly target selection.

Table 2 provides details on all targets observed during the course of the LEECH survey. Stellar masses were derived by fitting to PARSEC isochrones (Marigo et al. 2017) using the target age and photometry, except for the Field-B/A sublist for which mass and age were fit simultaneously (see Section 2.2). Magnitudes in the L'-band were derived using the $K-L'$ or $V-L'$ color spectral-type relations of Bessell & Brett (1988).

Figure 2 provides a graphical summary of some of the most relevant target parameters. Our median target age is 400 Myr (driven by the UMa sample), and our median distance is 25 pc. For comparison, the median target in the Rameau et al. (2013) survey is 30 Myr at 40 pc, and the median target in the International Deep Planet Survey (Galicher et al. 2016) is 120 Myr at 45 pc.

2.2. Age Determination for the Field-B/A Sublist

We constructed the Field-B/A sublist by querying the union of the Tycho2 and *Hipparcos* catalogs for stars observable from the LBT ($\delta > -20°$) with $B-V < 0.33$. We required target distances to be less than 30 pc for stars with $B-V \geqslant 0$ (A-type stars) and less than 55 pc for stars with $B-V < 0$ (B-type stars), accommodating the relatively low frequency of the more massive type. Two white dwarfs and all of the objects with pre-*Gaia* distance measurements uncertain at $\geqslant$5% were removed.

We closely followed the work of Nielsen et al. (2013) to determine an age for each observed target in the Field-B/A sublist, incorporating knowledge of the local stellar population to implement a Bayesian approach to derive a posterior distribution function of age (t_*), mass (M_*), and the log of the metallicity ratio with respect to the Sun (z_*).

Explicitly, we calculated a likelihood function for each target according to

$$P(V, (B-V)|t_*, M_*, z_*) \propto e^{-\frac{1}{2}\chi^2(t_*, M_*, z_*)}, \quad (1)$$

with

$$\chi^2(t_*, M_*, z_*) = \frac{(V-V_{\rm m})^2}{\sigma_V^2} + \frac{((B-V)-(B-V)_{\rm m})^2}{\sigma_{(B-V)}^2}. \quad (2)$$

In Equation (2), V and $(B-V)$ are, respectively, the observed absolute V-band magnitude and the $B-V$ color from the extended *Hipparcos* catalog (Anderson & Francis 2012). Both $V_{\rm m}$ and $(B-V)_m$ are functions of t_*, M_*, and z_*, and are the model predictions for absolute V-band magnitude and $B-V$ color from the PARSEC isochrones (Marigo et al. 2017). Since the extended *Hipparcos* compilation does not include an uncertainty entry for the absolute V-band magnitude, we

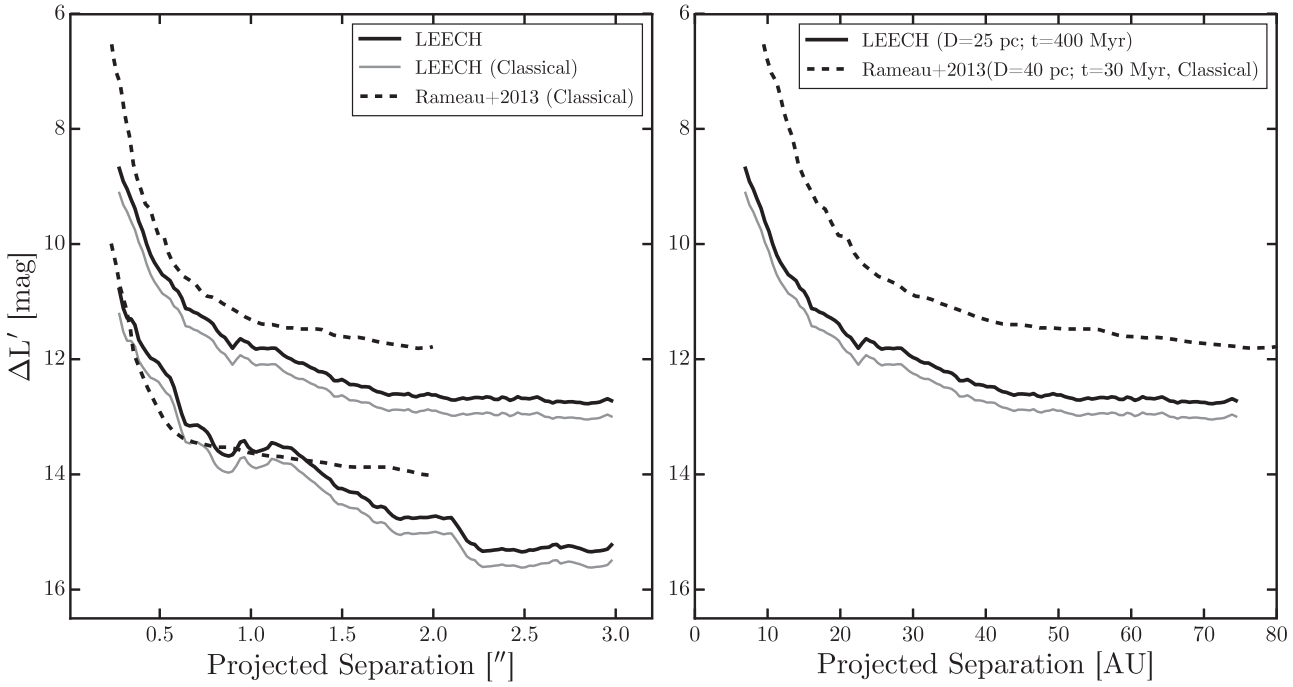

Figure 1. The median and best LEECH contrast curves and comparison curves from the L' direct imaging survey by Rameau et al. (2013). Left: contrast as a function of projected angular separation. We show two sets of contrast curves for the LEECH survey. With black solid lines, we show the contrast curves generated using a more modern approach that more carefully quantifies our confidence limits. With gray lines we show our LEECH contrast curves using a classical 5σ definition. The gray curves can be directly compared to the black dashed curves representing the Rameau et al. (2013) survey performance. Right: contrast vs. projected separation in astronomical units for a median contrast at each survey's median distance. A typical target for the LEECH survey is closer by, so we probe deeper at similar physical separations.

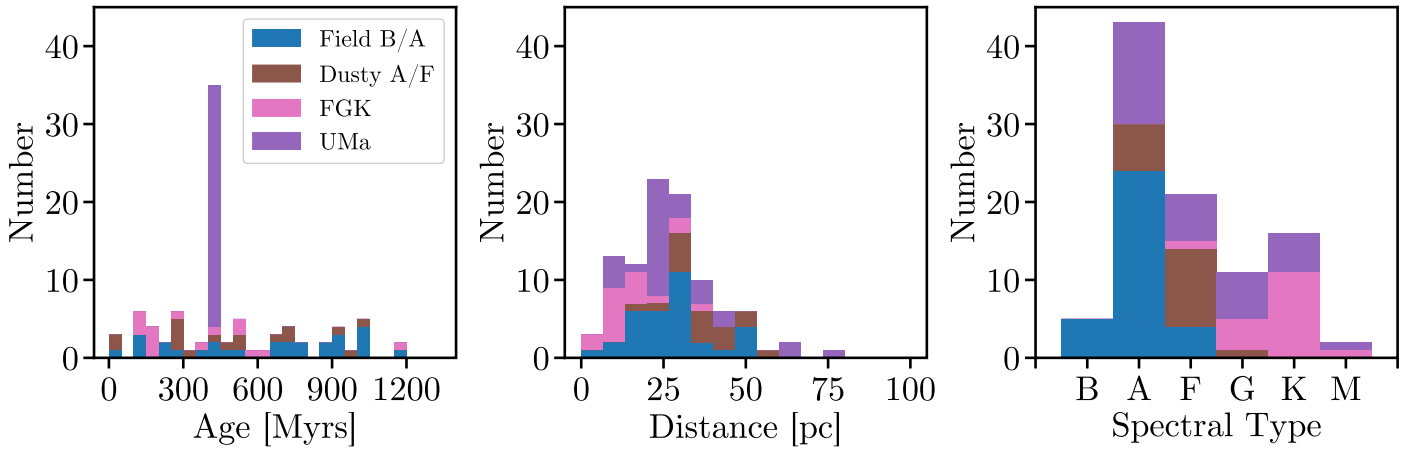

Figure 2. Age, distance, and spectral-type distributions for our LEECH targets. The large peak in the age distribution is due to our UMa subsample of similarly aged stars.

estimated σ_V by combining a propagation of the distance uncertainty with $1/\sqrt{2}$ times $\sigma_{(B-V)}$, the error on the measured $B-V$ color.

To derive our posterior distribution, we used a prior that is uncorrelated between the model parameters,

$$P(t_*, M_*, z_*) = P(t_*)P(M_*)P(z_*). \quad (3)$$

We used a uniform prior in linear age. This implies a constant star formation rate over an age range that includes all of our targets, which is consistent with the results of Cignoni et al. (2006). Like in Nielsen et al. (2013), our isochrone grid is logarithmic in age. Our prior accounts for the different linear age intervals represented by each grid point with the effect of pushing fits to older ages, where grid steps are wider. For the mass, we assumed a Salpeter initial mass function $dN/dM \propto M^{-2.35}$ (Salpeter 1955), with the effect of pushing fits to lower masses. Finally, for metallicity, we were again guided by Nielsen et al. (2013) and approximated the results of Casagrande et al. (2011) and Nieva & Przybilla (2012) by taking the metallicity distribution of nearby stars to be Gaussian distributed with mean −0.05 and σ 0.11 dex.

In Table 3, we summarize our Bayesian fitting results. For each parameter, we report the peak of the marginalized posterior probability distribution as the best fit. We also report

Table 2
Target Summary

Name	Name	R.A.	Decl.	Dist. (pc)	V (mag)	K (mag)	SpT	L' (mag)	Age[a] (Myr)	Mass ($M_\odot$)	Sublist
HIP 544[b]	HD 166	00 06 36	+29 01 17	13.78	6.13	4.31	K0V	4.25	155	0.95	FGK
HIP 1473	σ And	00 18 19	+36 47 06	42.03	4.52	4.38	A2V	4.37	450	2.10	Dusty-A
HIP 2843	HD 3296	00 36 01	−05 34 14	44.90	6.71	5.59	F6V	5.55	1000	1.35	Dusty-F
HIP 6061	f Psc	01 17 47	+03 36 52	78.25	5.14	4.92	A1V	4.92	412	2.52	UMa
HIP 8486[c]	EZ Cet	01 49 23	−10 42 13	23.67	6.75	5.15	G3V	5.10	412	1.05	UMa
HIP 8497	χ Cet	01 49 35	−10 41 11	23.28	4.68	3.87	F0V	3.84	412	1.55	UMa
HIP 8832[d]	γ Ari	01 53 31	+19 17 37	50.05	4.52	4.7	A3m	4.50	50	2.17	Field-A
HIP 8903[c]	β Ari	01 54 38	+20 48 28	17.99	2.65	2.38	A5V	2.36	931	2.08	Field-A
HIP 10064[c]	β Tri	02 09 32	+34 59 14	38.90	3.00	2.66	A5III	2.64	730	2.39	Dusty-A
HIP 10552[c]	HD 13959	02 15 53	+06 37 34	35.93	9.07	6.31	K4V	6.21	412	0.85	UMa
HIP 12828[c]	μ Cet	02 44 56	+10 06 50	26.50	4.20	3.46	A9III	3.43	1520	1.73	Field-A
HIP 13402[b]	HD 17925	02 52 32	−12 46 10	10.36	6.05	4.06	K1V	3.99	100	0.85	FGK
HIP 14576[c]	β Per	03 08 10	+40 57 20	27.57	2.12	2.08	B8V	2.08	447	3.48	Field-B
HIP 15457[b]	kap01 Cet	03 19 21	+03 22 12	9.15	4.85	3.34	G5V	3.29	400	1.00	FGK
HIP 16537[b]	ϵ Eri	03 32 55	−09 27 29	3.20	3.73	1.67	K2V	1.60	560	0.85	FGK
HIP 18859	HD 25457	04 02 3	−00 16 0	18.77	5.38	4.18	F7/8V	4.14	100	1.25	FGK
HIP 19859	HD 26923	04 15 28	+06 11 12	22.08	6.30	4.90	G0IV	4.85	412	1.10	UMa
HIP 19990	ω02 Tau	04 17 15	+20 34 42	29.31	4.91	4.36	A3m	4.35	1010	1.65	Field-A
HIP 20901	b Tau	04 28 50	+13 02 51	48.57	5.01	4.53	A5m	4.50	680	1.95	Dusty-A
HIP 21547	c Eri	04 37 36	−02 28 24	29.78	5.21	4.54	F0IV	4.51	791	1.55	Field-A
HIP 22845[b]	π.01 Ori	04 54 53	+10 09 02	34.23	4.65	4.42	A0V	4.42	10	1.85	Dusty-A
HIP 23875	β Eri	05 07 50	−05 05 11	27.40	2.79	2.38	A3IV	2.37	791	2.60	Field-A
HIP 25428	β Tau	05 26 17	+28 36 26	41.05	1.65	2.03	B7III	2.03	122	4.07	Field-B
HIP 25486[c]	AF Lep	05 27 04	−11 54 03	26.87	6.30	4.93	F8V	4.88	40	1.20	Dusty-F
HIP 26779[b]	HD 37394	05 41 20	+53 28 51	12.28	6.23	4.27	K1V	4.21	520	0.90	FGK
HIP 27072	γ Lep	05 44 27	−22 26 54	8.88	3.60	2.41	F6V	2.37	412	1.25	UMa
HIP 27913[b], c	χ01 Ori	05 54 22	+20 16 34	8.84	4.40	2.99	G0V	2.94	412	1.10	UMa
HIP 28360	β Aur	05 59 31	+44 56 50	24.87	1.90	1.86	A1IV-V	1.86	412	2.79	UMa
HIP 28954[b]	V1386 Ori	06 06 40	+15 32 31	15.78	6.74	4.82	K0V	4.76	600	0.90	FGK
HIP 33202	e Gem	06 54 38	+13 10 40	29.48	4.71	…	A8V	4.11	1650	1.60	Field-A
BD+201790	BD+20 1790	07 23 43	+20 24 58	27.79	10.00	6.88	K5	6.77	180	0.70	FGK
HIP 36188	β CMi	07 27 09	+08 17 21	49.14	2.89	3.03	B8V	3.03	215	3.40	Field-B
HIP 36704	HD 59747	07 33 00	+37 01 47	20.68	7.70	5.59	G5V	5.54	412	0.85	UMa
HIP 41152	HD 70313	08 23 48	+53 13 10	52.11	5.54	5.25	A3V	5.24	250	1.90	Dusty-A
HIP 41820[c]	CCDM J08316 + 3458AB	08 31 35	+34 57 58	27.32	7.51	…	G5V	5.88	412	0.95	UMa
HIP 42438[b]	π.01 UMa	08 39 11	+65 01 15	14.45	5.64	4.17	G1.5V	4.12	412	1.05	UMa
HIP 43625	HD 75616	08 53 06	+52 23 24	35.83	6.99	5.68	F5	5.64	400	1.20	Dusty-F
HIP 44127[d]	ι UMa	08 59 12	+48 02 30	14.16	3.14	2.66	A7V	2.63	1010	1.62	Field-A
HIP 44458[d]	HD 77407	09 03 27	+37 50 27	30.21	7.04	5.44	G0V	5.39	100	1.11	FGK
HD 78141	HD 78141	09 07 18	+22 52 21	25.30	7.98	5.78	K0	5.72	150	0.90	FGK
HIP 44897	HD 78366	09 08 51	+33 52 55	19.04	5.90	4.55	G0IV-V	4.50	950	1.10	Dusty-F
HIP 44901	f UMa	09 08 52	+51 36 16	27.14	4.48	3.81	A3m	3.77	1400	1.69	Field-A
HIP 46580	HD 82106	09 29 54	+05 39 18	12.78	7.20	4.79	K3V	4.70	370	0.80	FGK
HIP 48341	6 Sex	09 51 14	−04 14 36	65.23	6.02	5.64	A4V	5.62	412	1.89	UMa
HIP 49593	21 LMi	10 07 25	+35 14 40	27.01	4.49	4.00	A7V	3.97	412	1.70	UMa
HIP 49669[c]	α Leo	10 08 22	+11 58 01	24.31	1.40	1.62	B8IV	1.62	253	3.80	Field-B
HIP 53910	β UMa	11 01 50	+56 22 56	29.59	2.37	2.35	A1IV	2.34	412	2.76	UMa
HIP 53985[b]	DS Leo	11 02 38	+21 58 01	11.94	9.57	5.69	M1V	5.48	412	0.55	UMa
HIP 54872	δ Leo	11 14 06	+20 31 25	17.91	2.53	2.24	A5IV	2.22	858	2.05	Field-A
HIP 56997	61 UMa	11 41 03	+34 12 05	9.58	5.34	3.59	G8V	3.53	1200	0.94	FGK
HIP 57632	β Leo	11 49 03	+14 34 19	11.00	2.13	1.90	A3Va	1.89	412	1.95	Field-A
HIP 58001[c]	γ UMa	11 53 49	+53 41 41	33.91	2.44	2.33	A0V	2.33	412	2.82	UMa
HIP 58876	HD 104860	12 04 33	+66 20 11	45.21	7.91	6.50	F8	6.46	250	1.10	Dusty-F
HIP 59774	δ UMa	12 15 25	+57 01 57	24.85	3.32	3.09	A2V	3.08	412	2.19	UMa
HIP 61481	DO CVn	12 35 51	+51 13 17	26.25	8.54	…	K0	6.52	412	0.80	UMa
HIP 61946	HD 110463	12 41 44	+55 43 28	22.73	8.28	6.00	K3V	5.92	412	0.80	UMa
HIP 61960	ρ Vir	12 41 53	+10 14 08	38.17	4.88	4.68	A0V	4.68	500	1.80	Dusty-A
HIP 62512[c]	HD 111456	12 48 39	+60 19 11	26.18	5.83	4.55	F6V	4.51	412	1.30	UMa
HIP 62933	41 Vir	12 53 49	+12 25 06	60.72	6.24	5.47	A7III	5.44	412	1.75	UMa
HIP 62956	ϵ UMa	12 54 01	+55 57 35	24.26	1.77	1.76	A1III-IV	1.76	412	2.79	UMa
HIP 63076	8 Dra	12 55 28	+65 26 18	29.39	5.22	4.43	A7m	4.40	250	1.52	Dusty-F
HIP 63125	α02 CVn	12 56 01	+38 19 06	37.64	2.88	3.16	A0V	3.16	112	2.71	Field-B
HIP 63503[d]	78 UMa	13 00 43	+56 21 58	25.52	4.93	3.95	F2V	3.92	412	1.55	UMa

Table 2
(Continued)

Name	Name	R.A.	Decl.	Dist. (pc)	V (mag)	K (mag)	SpT	L' (mag)	Age[a] (Myr)	Mass ($M_\odot$)	Sublist
HIP 65327	HD 238224	13 23 23	+57 54 22	24.11	9.56	6.42	K5V	6.31	412	0.70	UMa
HIP 65378[c]	ζ UMa	13 23 55	+54 55 31	26.31	2.27	⋯	A1.5V	2.16	412	2.67	UMa
HIP 66459[b]	BD+36 2393	13 37 28	+35 43 03	10.96	9.07	5.49	K7.5V	5.35	412	0.60	UMa
HIP 69713	ι Boo	14 16 09	+51 22 02	29.15	4.75	4.29	A7V	4.26	1010	1.70	Field-A
HIP 69732	λ Boo	14 16 23	+46 05 17	30.34	4.18	3.91	A0V	3.91	290	2.00	Dusty-A
HIP 69989	18 Boo	14 19 16	+13 00 15	26.23	5.40	4.39	F5IV	4.35	412	1.40	UMa
HIP 71075	γ Boo	14 32 04	+38 18 29	26.74	3.02	2.56	A7IV	2.53	858	2.03	Field-A
HIP 71876	DL Dra	14 42 03	+61 15 42	41.24	6.25	⋯	F2V	5.40	412	1.40	UMa
HIP 72603[c]	α01 Lib	14 50 41	−15 59 50	23.37	5.16	4.14	F3V	4.11	300	1.40	Dusty-F
HIP 72659[d]	ξ Boo	14 51 23	+19 06 01	6.73	4.59	1.97	G7V	1.92	290	1.00	FGK
HIP 72848[c]	DE Boo	14 53 23	+19 09 10	11.38	6.01	4.32	K0.5V	4.26	1300	0.90	FGK
HIP 74702	HD 135599	15 15 59	+00 47 46	15.82	6.91	4.96	K0V	4.90	1300	0.85	FGK
HIP 76267[c]	α CrB	15 34 41	+26 42 52	23.01	2.24	2.21	A1IV	2.21	412	2.60	UMa
HIP 77233	β Ser	15 46 11	+15 25 18	46.66	3.67	3.42	A2IV	3.41	412	2.67	UMa
HIP 77622	ϵ Ser	15 50 48	+04 28 39	20.80	3.69	3.42	A5m	3.40	672	1.75	Field-A
HIP 80459[b]	G 202-48	16 25 24	+54 18 14	6.47	10.17	5.83	M1.5V	5.61	500	0.40	FGK
HIP 83207[c]	ϵ Her	17 00 17	+30 55 35	50.08	3.92	3.92	A0V	3.92	215	2.91	Field-B
HIP 84379	δ Her	17 15 01	+24 50 21	23.33	3.13	2.85	A1IV	2.84	729	2.25	Field-A
HIP 85829[c]	ν.02 Dra	17 32 16	+55 10 22	29.98	4.83	4.16	A4m	4.13	700	1.62	Dusty-A
HIP 86032[c]	α Oph	17 34 56	+12 33 36	14.90	2.07	1.66	A5III	1.64	931	2.10	Field-A
HIP 88771	72 Oph	18 07 20	+09 33 49	26.81	3.73	3.42	A5V	3.40	931	2.00	Field-A
HIP 91262	α Lyr	18 36 56	+38 47 01	7.68	0.03	0.13	A0V	0.13	485	2.41	Field-A
HIP 92161	111 Her	18 47 01	+18 10 53	28.29	4.36	4.08	A5III	4.06	672	1.85	Field-A
HIP 93408	16 Lyr	19 01 26	+46 56 05	38.61	5.01	4.51	A6IV	4.48	412	1.85	UMa
HIP 93747	ζ Aql	19 05 24	+13 51 48	23.52	2.99	2.88	A0IV-V	2.88	526	2.60	Field-A
HIP 93805	λ Aql	19 06 14	−04 52 57	36.95	3.43	3.65	B9V	3.65	122	2.66	Field-B
HIP 97165[d]	δ Cyg	19 44 58	+45 07 50	51.26	2.87	2.83	A0IV	2.83	350	3.14	Field-B
HIP 97649	α Aql	19 50 46	+08 52 05	5.13	0.76	0.24	A7V	0.21	1010	1.70	Field-A
HIP 105199	α Cep	21 18 34	+62 35 08	15.04	2.46	2.07	A8V	2.04	1190	2.20	Field-A
HIP 105918	HD 204277	21 27 06	+16 07 26	33.11	6.72	5.45	F8V	5.41	900	1.18	Dusty-F
HIP 107556[c]	δ Cap	21 47 02	−16 07 38	13.63	2.83	2.14	A5m	2.11	1400	1.61	Field-A
HIP 109427	θ Peg	22 10 11	+06 11 52	27.20	3.55	3.33	A1V	3.32	729	2.10	Field-A
BD+483686	V383 Lac	22 20 07	+49 30 11	34.44	8.58	6.51	K1V	6.44	150	0.90	FGK
HIP 111278	39 Peg	22 32 35	+20 13 48	53.59	6.44	5.58	F1V	5.55	500	1.55	Dusty-F
HIP 114570	7 And	23 12 33	+49 24 22	24.40	4.52	3.77	F1V	3.74	1400	1.56	Field-A

Notes.
[a] Stellar ages for stars in the FGK subsample are from Mamajek & Hillenbrand (2008) and Heinze et al. (2010b). Ages for stars in the Dusty-A/F subsample are from Gáspár et al. (2013). Ages for stars in the UMa subsample are from Jones et al. (2015). Ages for stars in the Field-B/A subsample are derived in this work.
[b] Our photometric sensitivity was sufficient to detect $\leqslant 10\,M_{\rm Jup}$ cold-start planets in these systems.
[c] Close ($\lesssim 1''$) binary systems.
[d] Wide ($\gtrsim 1''$) binary systems.

the parameter ranges corresponding to the intervals between 16% and 84% and between 2.5% and 97.5% in the cumulative distribution function of the posterior.

One of the targets in our Field-B/A sublist, HIP 25428, is actually a high-confidence (96%) member of the AB Dor moving group based on its kinematics according to the online BANYAN Σ Bayesian analysis tool (Gagné et al. 2018). The AB Dor moving group has an age of 149^{+51}_{-19} Myr (Bell et al. 2015). We derive an age of 122 Myr for HIP 25428 with 95% confidence range due to statistical uncertainty ranging from 104 to 124 Myr. We show below that significant systematic uncertainty (∼50%) is also involved in age-dating stars with model isochrone fitting. Thus, we take our fitted value as validation that our approach returns sensible results. Another target, HIP 57632 (β Leo), is often reported to have an age of ∼40 Myr based on assumed membership in either IC 2391 (Eggen 1991) or the Argus Association (Zuckerman et al. 2011). Our best-fit age of 412 Myr is in some tension with the younger age. However, other authors also derive an older age for HIP 57632: Nielsen et al. (2013) find a 95% confidence interval of 16–458 Myr, and Rieke et al. (2005) find a best-fit age of 520 Myr. While our age determination for HIP 57632 is highly uncertain (56–685 Myr, 95% confidence), the older ages may not be incorrect. The BANYAN Σ tool reports 0% probability of HIP 57632 membership in IC 2391 and leaves out an analysis of the Argus Association as this may not be a co-eval group of stars (Bell et al. 2015). HIP 57632 hosts a debris disk, but, as shown by Rieke et al. (2005), the 24 μm flux excess is not inconsistent with the upper envelope of debris-disk luminosities for an age of 520 Myr.

In all, we share six targets with Nielsen et al. (2013), who used the Siess et al. (2000) isochrones to perform their fits. We plot our derived ages versus the Nielsen et al. (2013) ages in Figure 3. Error bars show the corresponding 95% confidence intervals. From left to right, the objects are HIP 93805, HIP 36188, HIP 49669, HIP 57632, HIP 54872, and HIP 107556. The ages

Table 3
Best-fit Age, Mass, and Metallicity for Observed Stars in the Field-B/A Sublist

Name	Age [Myr]					Mass [$M_\odot$]					Metallicity [$\log_{10}(z/z_\odot)$]				
	Mode	16%–84%		2.5%–97.5%		Mode	16%–84%		2.5%–97.5%		Mode	16%–84%		2.5%–97.5%	
HIP 8832	50	14	81	7	151	2.2	2.1	2.3	2.1	2.3	−0.26	−0.27	−0.13	−0.30	−0.04
HIP 8903	931	808	989	704	5477	1.9	1.9	2.0	1.8	2.0	−0.04	−0.14	0.05	−0.25	0.18
HIP 12828	1517	1249	1629	1045	1773	1.6	1.5	1.6	1.5	1.7	−0.05	−0.15	0.06	−0.23	0.17
HIP 14576	447	389	438	373	465	2.8	2.7	2.8	2.6	2.9	0.03	−0.15	0.05	−0.24	0.17
HIP 19990	1010	403	1095	108	1358	1.5	1.5	1.6	1.4	1.6	−0.03	−0.15	0.06	−0.24	0.13
HIP 21547	791	190	937	44	1265	1.5	1.4	1.5	1.4	1.5	−0.04	−0.16	−0.01	−0.25	0.04
HIP 23875	791	689	776	662	820	2.2	2.2	2.3	2.1	2.3	−0.10	−0.11	0.05	−0.27	0.19
HIP 25428	122	106	119	104	124	4.5	4.4	4.5	4.3	4.5	−0.14	−0.19	0.07	−0.27	0.17
HIP 33202	1646	1159	1723	834	1919	1.5	1.5	1.6	1.4	1.6	−0.05	−0.15	0.06	−0.24	0.17
HIP 36188	215	174	223	151	247	3.5	3.3	3.6	3.2	3.7	−0.05	−0.15	0.06	−0.25	0.17
HIP 44127	1010	606	1086	346	1284	1.6	1.6	1.7	1.5	1.7	−0.06	−0.15	0.06	−0.24	0.17
HIP 44901	1399	1131	1516	932	1686	1.6	1.6	1.7	1.5	1.7	−0.03	−0.15	0.06	−0.25	0.17
HIP 49669	253	179	255	138	287	3.3	3.2	3.5	3.1	3.8	−0.03	−0.15	0.06	−0.25	0.17
HIP 54872	858	704	898	606	982	1.9	1.9	2.0	1.8	2.1	−0.05	−0.15	0.07	−0.25	0.17
HIP 57632	412	200	530	56	685	1.8	1.8	1.9	1.7	1.9	−0.11	−0.16	0.05	−0.26	0.13
HIP 62956	380	357	399	345	411	2.9	2.7	2.9	2.7	3.0	0.02	−0.15	0.03	−0.17	0.19
HIP 63076	1010	319	1160	72	1483	1.5	1.4	1.5	1.4	1.5	−0.06	−0.15	0.04	−0.24	0.09
HIP 63125	112	47	126	19	166	3.4	3.2	3.5	3.1	3.7	−0.05	−0.16	0.05	−0.25	0.15
HIP 69713	1010	492	1102	169	1357	1.6	1.5	1.6	1.5	1.7	−0.04	−0.15	0.06	−0.24	0.16
HIP 71075	858	799	903	732	927	2.1	2.0	2.1	2.0	2.2	0.02	−0.15	0.03	−0.17	0.17
HIP 77622	672	391	782	190	952	1.7	1.7	1.8	1.6	1.9	−0.05	−0.15	0.06	−0.25	0.17
HIP 83207	447	389	477	341	516	2.5	2.4	2.5	2.3	2.6	−0.02	−0.14	0.06	−0.25	0.17
HIP 84379	729	565	759	464	835	2.0	1.9	2.1	1.9	2.1	−0.08	−0.15	0.06	−0.23	0.16
HIP 86032	931	781	952	690	1468	1.9	1.9	2.0	1.8	2.1	−0.08	−0.17	0.09	−0.28	0.17
HIP 88771	931	755	991	633	1079	1.8	1.8	1.9	1.8	2.0	−0.06	−0.14	0.06	−0.23	0.16
HIP 91262	485	431	525	380	565	2.4	2.3	2.4	2.3	2.5	0.01	−0.16	0.07	−0.24	0.17
HIP 92161	672	408	785	210	944	1.7	1.7	1.8	1.6	1.9	−0.04	−0.15	0.06	−0.25	0.17
HIP 93747	526	428	563	357	616	2.2	2.2	2.3	2.1	2.3	−0.05	−0.14	0.06	−0.23	0.16
HIP 93805	122	54	143	21	188	3.0	2.9	3.1	2.8	3.2	−0.06	−0.16	0.05	−0.25	0.15
HIP 97165	350	247	345	235	350	3.1	3.1	3.3	3.0	3.4	0.04	−0.15	0.07	−0.27	0.12
HIP 97649	1010	690	1141	454	1330	1.6	1.6	1.7	1.5	1.8	−0.05	−0.15	0.06	−0.24	0.17
HIP 105199	1188	1045	1244	942	2358	1.8	1.8	1.9	1.7	1.9	−0.04	−0.16	0.06	−0.28	0.16
HIP 107556	1399	256	1633	47	2280	1.6	1.5	1.6	1.4	1.7	−0.06	−0.17	0.04	−0.26	0.14
HIP 109427	729	594	775	500	845	2.0	2.0	2.1	1.9	2.1	−0.11	−0.12	0.07	−0.22	0.17
HIP 114570	1399	927	1553	571	1778	1.5	1.5	1.6	1.4	1.6	−0.05	−0.15	0.07	−0.24	0.17

we derive are systematically older than the ages derived by Nielsen et al. (2013). For the stars common to both studies, the Nielsen et al. (2013) ages are 50% younger than LEECH ages, on average. This suggests the magnitude of systematic error inherent in the model isochrones. The different inferred ages may be due to differences in the treatment of mixing within stars (e.g., overshoot in the convective core), which can prolong main-sequence lifetimes. By pushing targets to older ages, our models are more conservative because we have less sensitivity to planets around older stars.

3. Observations

Our survey was conducted using the LBTI instrument (Hinz et al. 2016) at the LBT on Mt. Graham in southern Arizona. LBTI is located between the two 8.4 m primary mirrors of the LBT at the combined bent Gregorian focus. Light from each side of the telescope is corrected for atmospheric aberrations using the LBTI AO system (Bailey et al. 2014) and delivered into the instrument via a cryogenic beam combiner where it is then directed to individual science modules. For LEECH observations, we used the LMIRcam module of LBTI, which is optimized for work in the thermal–infrared (3–5 μm; Skrutskie et al. 2010; Leisenring et al. 2012). LBTI does not include an instrument derotator, so images always rotate with respect to the detector pixels as the parallactic angle changes.

During the course of the LEECH survey, LMIRcam provided an $11'' \times 11''$ field of view, reading a 1024×1024 subsection of its 5.2 μm cutoff HAWAII-2RG detector (the full 2048×2048 extent of the array now provides a $20'' \times 20''$ field of view with LMIRcam). LMIRcam was designed with a plate scale to accommodate imaging interferometry at the full resolution of the 23 m LBT (10.7 mas pixel^{-1}). However, for LEECH observations, we operated without overlapping and interfering the beams of the two primary mirrors, opting to make two images of each source on the detector instead. In this mode, the L' images from each side were oversampled, providing added robustness to bad pixels and cosmic rays.

Our simultaneous non-overlapped imaging strategy provided increased sensitivity in speckle-limited regimes because each image displays a mostly independent speckle pattern. However, in the background-limited regime, our sensitivity was decreased because of the presence of two sky backgrounds per image.

Our standard observing procedure aligned both images of a target star in the upper section of the detector keeping each image $3''$ from the edge of the detector and leaving $5''$ between

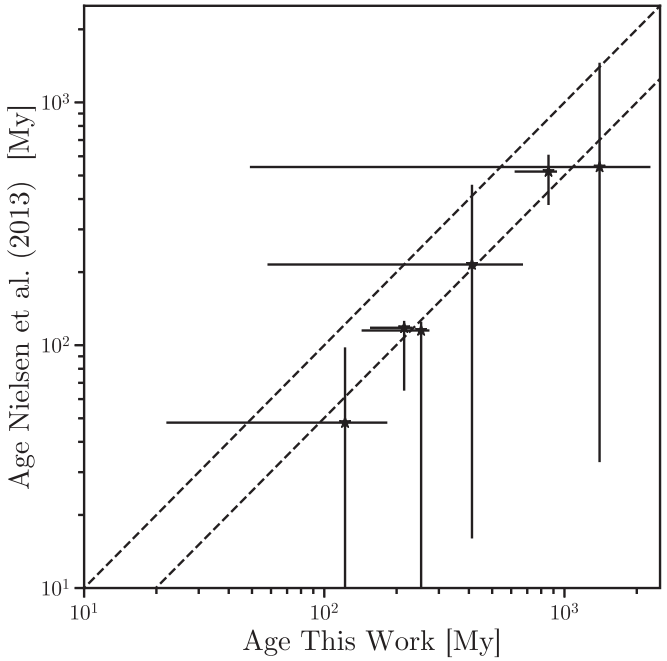

Figure 3. Ages derived here vs. ages derived by Nielsen et al. (2013) for the six targets shared by both surveys. From left to right, the target stars are HIP 93805, HIP 36188, HIP 49669, HIP 57632, HIP 54872, and HIP 107556. The upper dashed line indicates a one-to-one relationship, the lower dashed line one-to-two. Our age estimates are systematically older than those found by Nielsen et al. (2013), suggesting the magnitude of systematic error inherent to the model isochrones.

the images. For some very nearby targets (e.g., Vega, Altair), we used only one side of the telescope and created only one centered image in order to maximize our field of view. We also performed single-sided observations during intervals of technical downtime affecting either of the AO systems. In particular, all observations conducted during the spring of 2013 were made with the left side of the telescope only.

We collected data using an up–down nod pattern (left–right for some of our single-sided observations of binary systems) to track low spatial frequency variations in the sky background level, and high and low spatial frequency detector drifts. A typical sequence included 50 frames in each position each composed of three coadds of 0.3 s exposures. Our exposure time was set to balance image saturation and detector readout efficiency. Our choice of exposure time generally resulted in a saturated core in each of our stellar images. (We do not use a coronagraph for LEECH observations.) Our nod frequency was set to optimize on-sky efficiency given the demands of a variable background and detector.

An observing log for the LEECH survey is presented in Table 4. Differences in exposure time and rotation angle between the two sides of LBT can result from differences in the AO performance (poor Strehl/open AO loop) that cause some frames to be rejected for one side but not the other (see Section 4).

4. Data Reduction and Processing

4.1. Basic Image Processing

We use a bad-pixel mask to identify pixels with persistent problems and correct them using the median of the nearest eight good pixels. LMIRcam images exhibit low-level time-variable

Table 4
LEECH Observing Log

Name	Date	Seeing[a] (″)	Left Side t_{int} (s)	Left Side Rot. (°)	Right Side t_{int} (s)	Right Side Rot. (°)
HIP 54872	2013 Apr 18	1.7 ± 0.2	2043	67	…	…
HIP 69713	2013 Apr 18	2.0 ± 0.2	1638	53	…	…
HIP 86032	2013 Apr 18	1.4 ± 0.2	1716	17	…	…
HIP 88771	2013 Apr 19	1.2	1256	17	…	…
HIP 77622	2013 Apr 19	1.2	10	0	…	…
HIP 76267	2013 Apr 20	0.9 ± 0.1	1979	107	…	…
HIP 66459	2013 Apr 20	0.9 ± 0.1	2440	161	…	…
HIP 42438	2013 Apr 21	0.9 ± 0.2	4199	48	…	…
HIP 84379	2013 Apr 21	0.9 ± 0.1	3153	96	…	…
HIP 46580	2013 Apr 22	1.1 ± 0.2	3276	51	…	…
HIP 72659	2013 Apr 22	0.9 ± 0.1	1909	45	…	…
HIP 62512	2013 Apr 22	1.2 ± 0.2	3197	38	…	…
HIP 49593	2013 Apr 23	1.0	3271	158	…	…
HIP 93408	2013 Apr 23	1.0 ± 0.1	975	6	…	…
HIP 61946	2013 Apr 23	0.9 ± 0.1	4738	68	…	…
HIP 83207	2013 Apr 24	0.8	2635	150	…	…
HIP 57632	2013 Apr 24	1.2 ± 0.2	3333	61	…	…
HIP 72659	2013 Apr 24	0.8 ± 0.1	1965	34	…	…
HIP 62512	2013 Apr 24	0.9 ± 0.1	1465	14	…	…
HIP 65378	2013 Apr 26	1.1 ± 0.2	…	…	4599	63
HIP 77233	2013 Apr 26	0.8 ± 0.1	3872	44	…	…
HIP 92161	2013 Apr 26	0.7	…	…	4124	58
HIP 69713	2013 May 23	0.8 ± 0.0	3073	96	…	…
HIP 93408	2013 May 23	0.7	175	0	…	…
HIP 97649	2013 May 24	0.9 ± 0.2	2873	83	…	…
HIP 69989	2013 May 25	0.9 ± 0.1	2468	75	…	…
HIP 77622	2013 May 25	0.9 ± 0.1	2285	47	…	…
HIP 93747	2013 Jun 17	1.0 ± 0.1	1220	66	…	…
HIP 72659	2013 Jun 17	0.9 ± 0.1	3012	82	…	…
HIP 71876	2013 Jun 26	0.8 ± 0.1	1611	47	…	…
HIP 72848	2013 Jun 27	0.9 ± 0.1	2708	69	…	…
HIP 91262	2013 Jun 27	0.6	…	…	…	…
HIP 105199	2013 Oct 18	1.1 ± 0.1	2534	42	2552	47
HIP 544	2013 Oct 18	1.0 ± 0.1	1475	133	1465	133
HIP 27072	2013 Oct 18	1.0 ± 0.1	846	15	859	15
HIP 27913	2013 Oct 20	0.9 ± 0.1	…	…	2054	44
HIP 18859	2013 Oct 21	0.8 ± 0.1	…	…	441	9
HIP 28954	2013 Oct 21	1.0 ± 0.1	4078	89	4037	82
HIP 8903	2013 Oct 22	1.1 ± 0.2	…	…	2374	75
HIP 19990	2013 Oct 23	1.0 ± 0.1	…	…	6675	117
HIP 26779	2013 Oct 24	0.9 ± 0.1	…	…	6048	117
HIP 14576	2013 Oct 24	0.9 ± 0.1	…	…	1652	51
HIP 42438	2013 Nov 19	1.4 ± 0.2	…	…	4197	74
HIP 25428	2013 Nov 20	1.1 ± 0.2	…	…	1125	120
HIP 53985	2013 Dec 24	1.0 ± 0.1	2499	75	2517	74
HIP 13402	2013 Dec 24	0.9 ± 0.1	3378	38	3395	26
HD 78141	2013 Dec 24	0.9 ± 0.0	1092	57	920	57
HIP 44901	2013 Dec 25	1.2 ± 0.1	3467	84	3493	83
HIP 53910	2013 Dec 25	1.0 ± 0.1	3376	63	3375	61
HIP 6061	2013 Dec 25	1.1 ± 0.2	3353	65	3383	65
HIP 10552	2013 Dec 26	2.0 ± 0.3	…	…	1685	34
HIP 58001	2013 Dec 26	2.0 ± 0.3	105	3	105	3
HIP 62933	2013 Dec 26	1.4 ± 0.3	3677	51	3691	44
HIP 44127	2013 Dec 26	1.8 ± 0.7	…	…	1870	28
HIP 28360	2013 Dec 27	1.4 ± 0.1	3018	86	3015	80
HIP 44458	2013 Dec 27	1.6	1760	89	1776	103
HIP 65327	2013 Dec 27	2.1 ± 0.4	2328	47	2296	47
HIP 8497	2013 Dec 27	1.8 ± 0.3	3401	44	3404	44
HIP 33202	2013 Dec 28	1.8 ± 0.5	3150	60	…	…
HIP 15457	2013 Dec 30	1.6 ± 0.2	2722	47	2713	47
HIP 66249	2013 Dec 30	2.0 ± 0.2	2161	64	…	…
HIP 36188	2013 Dec 30	1.6 ± 0.2	3028	54	3077	57

Table 4
(Continued)

Name	Date	Seeing[a] (″)	Left Side t_{int} (s)	Left Side Rot. (°)	Right Side t_{int} (s)	Right Side Rot. (°)
HIP 21547	2013 Dec 31	1.3 ± 0.2	2928	47	3017	47
BD+20 1790	2014 Feb 10	1.3 ± 0.1	1517	54	…	…
HIP 63076	2014 Feb 14	1.0 ± 0.1	3276	49	3272	50
HIP 72603	2014 Feb 14	1.4 ± 0.1	2649	25	2655	24
HIP 48341	2014 Feb 14	1.2 ± 0.1	4073	50	4066	42
HIP 25486	2014 Feb 14	1.2 ± 0.1	…	…	3330	32
HIP 80459	2014 Mar 12	0.9 ± 0.1	2002	41	1978	40
HIP 41152	2014 Mar 12	1.0 ± 0.1	2857	51	2857	50
HIP 58001	2014 Mar 12	1.4 ± 0.3	4078	49	4080	51
HIP 56997	2014 Mar 13	0.9	2419	169	2413	170
HIP 85829	2014 May 08	1.1 ± 0.1	2959	59	2953	56
HIP 69732	2014 May 08	1.3 ± 0.2	3994	117	4008	116
HIP 62956	2014 May 08	1.1 ± 0.2	2610	38	2612	38
HIP 61960	2014 May 09	1.1 ± 0.2	2038	47	…	…
HIP 72848	2014 May 09	1.0 ± 0.1	2643	75	…	…
HIP 91262	2014 May 09	0.9 ± 0.1	3683	158	…	…
HIP 107556	2014 Oct 04	0.7	3720	39	3615	39
HIP 16537	2014 Oct 04	0.7	3856	49	3822	48
HIP 8497	2014 Oct 04	0.6	3741	41	…	…
HIP 105199	2014 Oct 05	1.5 ± 0.2	4008	81	…	…
HIP 19859	2014 Oct 05	0.8 ± 0.1	2767	60	2764	60
BD+48 3686	2014 Oct 06	0.8 ± 0.1	3981	108	3980	108
HIP 105918	2014 Nov 06	1.3 ± 0.2	2209	44	…	…
HIP 2843	2014 Nov 06	1.7 ± 0.3	1375	45	…	…
HIP 111278	2014 Nov 08	1.1 ± 0.2	…	…	1782	54
HIP 8486	2014 Nov 08	1.2 ± 0.1	781	6	765	10
HIP 12828	2014 Nov 08	1.1 ± 0.2	2508	36	2509	32
HIP 36704	2014 Dec 11	0.8	4125	153	4128	153
HIP 1473	2014 Dec 11	1.0	1987	84	1989	86
HIP 10064	2015 Jan 05	0.9 ± 0.1	1463	146	1449	146
BD+20 1790	2015 Jan 05	0.8 ± 0.1	3481	80	3470	79
HIP 21547	2015 Jan 05	0.9 ± 0.1	2997	34	…	…
HIP 63125	2015 Jan 05	0.9	801	30	784	33
HIP 58876	2015 Jan 06	1.2 ± 0.1	3065	44	3052	44
HIP 20901	2015 Jan 06	1.0 ± 0.2	4794	79	4787	82
HIP 49669	2015 Jan 06	0.9 ± 0.1	3535	61	3539	58
BD+20 1790	2015 Jan 06	0.9 ± 0.1	3032	54	3017	55
HIP 23875	2015 Feb 08	0.9 ± 0.1	2208	121	2202	121
HIP 22845	2015 Feb 09	1.0 ± 0.2	3533	69	3595	65
HIP 41820	2015 Feb 09	1.6 ± 0.2	1593	106	1591	107
HIP 63503	2015 Mar 06	1.2 ± 0.2	1880	33	…	…
HIP 63503	2015 Mar 10	1.1 ± 0.2	2456	48	2457	49
HIP 74702	2015 Mar 10	1.5 ± 0.2	3599	65	3583	65
HIP 43625	2015 Mar 10	1.1 ± 0.1	3111	64	3108	76
HIP 97165	2015 Jun 11	1.2 ± 0.2	…	…	598	10
HIP 93805	2015 Jun 11	1.4 ± 0.1	839	29	836	28
HIP 109427	2015 Jun 12	0.9 ± 0.1	3222	45	3233	44
HD 106591	2015 Jun 12	1.0 ± 0.1	264	9	264	9
HIP 114570	2015 Jun 26	0.9 ± 0.1	…	…	1295	29
HIP 44897	2016 Mar 25	1.2 ± 0.2	3248	169	3241	169
HIP 71075	2016 Mar 26	1.3 ± 0.2	2753	25	2769	25
HIP 61481	2016 Mar 27	1.2 ± 0.2	2236	47	2233	47
HIP 61481	2017 Apr 05	1.1 ± 0.2	3121	56	3115	55

Note.
[a] Mean and standard deviation of the seeing as measured by the DIMM at LBT and recorded in image headers. For some data sets, seeing was unavailable in headers. For these we report the value written in the nightly observing log.

offsets in each 64 × 1024 pixel readout channel. We remove these offsets by subtracting the median pixel value from each channel after excluding all 3σ outliers. All images are corrected for distortion using a two-dimensional polynomial transformation and the coefficients reported by Maire et al. (2015). After distortion correction, image pixels are binned 2 × 2. Binning the oversampled frames reduces the influence of any cosmic-ray hits during the exposure and any bad pixels not represented in the mask.

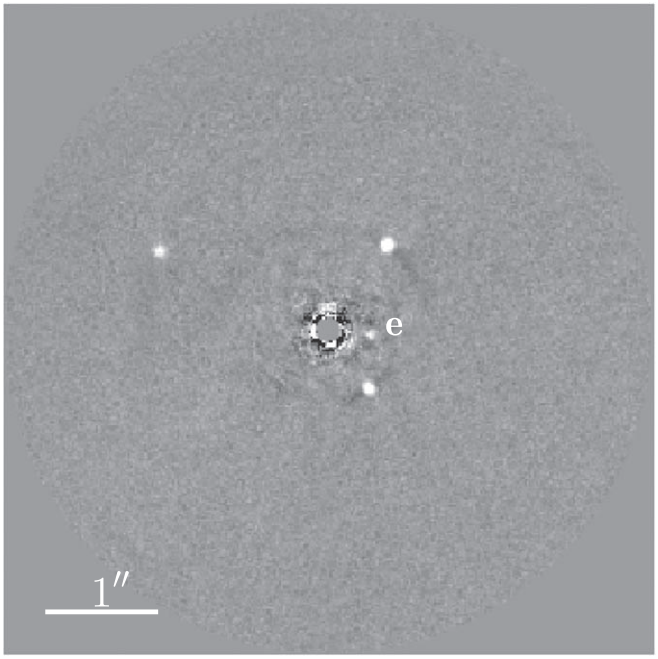

Figure 4. Demonstration of the functionality of our LEECH data processing pipeline on an HR 8799 data set. We detect all four directly imaged planets at high significance even though the data were collected using only one side of the telescope under poor conditions (seeing $\gtrsim$1.″5). The innermost planet "e" (labeled) is separated by less than 0.″4 and is detected with a signal-to-noise ratio of 7.5.

We remove variable sky background using nod subtraction. Although the left and right sides of the telescope are typically nodded together during dual-sided observations, nods on each side are fundamentally independent. Thus, we distinguish between the left and right image when performing nod subtraction. This gives us added flexibility to utilize frames when one side of the telescope is experiencing issues (e.g., an open AO loop).

After nod subtraction, each beam (left–up, left–down, right–up, right–down) is cropped to a 3″ radius field of view. Then, all images within a beam are co-aligned on a subpixel level using a cross-correlation with a median-combined image as a template. After shifting all images, the cross-correlation process is repeated with a new median template. Images with the least correlation with the second median image are discarded. This effectively filters images with poor Strehl ratio and open loop data. We typically reject the worst 10%–30% of images depending on the quality of the data and the AO-loop stability. Exposure times in Table 4 report the total retained data after culling.

4.2. High-contrast Image Processing

We reduce each nod position (up/down left/right) independently, combining the beams to produce a master image using a weighted mean as a last step. Keeping the positions separate produces similarly reduced subsets of our data that allow us to better distinguish real signals from time-variable speckles. In some

of our data sets, some nod positions exhibit diffraction rings from dust contamination on optics near the focal plane in LMIRcam. In these cases, our approach allows us to downweight the nod positions with contamination in order to maximize our contrast.

For each nod position, we combine the reduced images into groups with less than 2° of the parallactic angle change. This rotation limit is chosen so that a source at 3″ moves $\lesssim\lambda/D$. These combined images are then used in our principal component analysis (PCA)-based image processing algorithm.

In PCA-based image processing algorithms, the stellar point-spread function (PSF) and quasi-static speckles in each image are modeled as the projection onto the subspace spanned by the leading eigenimages of the pixel covariance matrix. We use all combined images as reference images for the application of PCA. The signal of a faint, rotating planet is not expected to be represented in one of the leading eigenimages. We measured our throughput on a typical double-sided data set and recovered 35% at 0.″5 and 68% at 2″ (21 (λ/D)). To put this in context, another commonly used high-contrast image processing algorithm—locally optimized combination of images (LOCI)—delivers ∼65% throughput at 35 (λ/D) (Lafrenière et al. 2007b).

Our approach works annulus by annulus in each image. We model annuli of 13 pixels (∼3(λ/D)) wide but subtract only the central 1 pixel wide ring for each radius. For each radius, the number of principal components we use to model the stellar PSF and speckle distribution is optimized to maximize the achieved contrast (see Section 4.3). After removing the image of the star, all images are derotated using the parallactic angle and the offset to true north reported in Maire et al. (2015). We then median-combined to enhance signal to noise.

4.3. Optimizing NPCs

For each radius, we determine the optimal number of principal components (NPCs) to subtract by injecting fake sources and maximizing the measured signal-to-noise ratio.

For the artificial source injections, we use unsaturated images of the primary star taken before and/or after our saturated imaging as a photometric standard and PSF model. Some of our targets do not have unsaturated frames saved as part of their data set. For these targets, we use unsaturated images of another star taken the same night or, in one case, we use the unsaturated image of an optical ghost that appears 5.76 mag fainter than the primary. We inject planets that rotate opposite the sky rotation in our frames and then reduce them using the opposite of the parallactic angle to derotate in the last step of our high-contrast image processing algorithm. This reduces our susceptibility to biases from real astrophysical signals in the data (e.g., Wahhaj et al. 2013).

We measure the signal-to-noise ratio of each artificial planet as follows. After PCA subtraction, we smooth the image with a Gaussian with the same width as our PSF and then take the peak pixel value in the vicinity of our injected source as the signal level. For a noise estimate, we process the image stack without injecting an artificial source but using the same NPCs and reverse rotation. We then smooth the image using the same kernel as before and take the noise level to be the standard deviation of pixel values within the 13 pixel wide annulus centered at the radius of the artificial planet.

In addition to optimizing the NPCs necessary at each radius, this process also automatically produces a 5σ contrast curve quantifying our photometric sensitivity as a function of radial separation from the host star. As discussed below, these contrast curves are improved when we combine nods and telescope apertures to create a final image for each target. In Section 5.2.1, we discuss the necessary adjustments to these contrast curves to account for the small number statistics at small separations. Since our contrast curves are created with artificial source injection, the effects of our algorithmic throughput are built in.

4.4. Combining Beams

At this point, we have up to four optimally reduced images and contrast curves for each data set (one for each nod position; there will be only two for single-sided data sets). We use a weighted sum to combine each of the separately reduced beams (up/down left/right) to make a final combined image and contrast curve. To find the best weights, for each radius, we inject a fake planet of the same magnitude into each beam at the same position. We then reduce all beams using the previously determined optimal NPCs. Finally, we grid-search for the weights to optimize the signal-to-noise ratio of the resulting summed image. Our final contrast curves for each target are constructed so that the combined contrast is scaled to reflect the increase in the signal-to-noise ratio after the weighted sum:

$$\Delta m(r)_{\rm comb} = \Delta m_i(r) + 2.5\log_{10}\left(\frac{\rm SNR_{comb}}{5}\right), \quad (4)$$

where $\Delta m_i(r)$ is the initial contrast that was the deepest measured among the beams, $\rm SNR_{comb}$ is the signal-to-noise ratio that resulted after the weighted combination, and $\Delta m(r)_{\rm comb}$ is our final contrast at radius r. In Figure 4, we show a fully reduced image of the HR 8799 system to demonstrate the performance of our pipeline. The HR 8799 data set was taken under poor conditions (seeing $\gtrsim$1.″5) on 2013 October 22 using only the right side of the LBT. The image includes 44 minutes of exposure time and tracks 80° of parallactic angle change. We detect the innermost planet, HR 8799 e—separated by $\lesssim$0.″4—with a signal-to-noise ratio of 7.5.

5. Results

5.1. Search for Planetary Companions

To search all of our final reduced images for new companions, we use both visual inspection and automated signal-to-noise maps. Our by-eye approach uses the individually reduced beam images as well as the final combined image for each target. This allows us to quickly discriminate between real objects and bright speckles because astrophysical sources should appear at the same position in each beam, albeit at a lower signal-to-noise ratio.

We automatically constructed signal-to-noise maps for each target by smoothing the final combined image to estimate signal strength on the scale of our PSF, and smoothing reverse-rotated final combined images to estimate the noise level in each annulus. We flagged and inspected each data set with at least 1 pixel above a signal-to-noise ratio of 4. These maps did not reveal any signals not previously flagged by our visual inspection. We did not discover any new exoplanets orbiting any of our targeted stars.

In the following subsections, we describe our findings in detail.

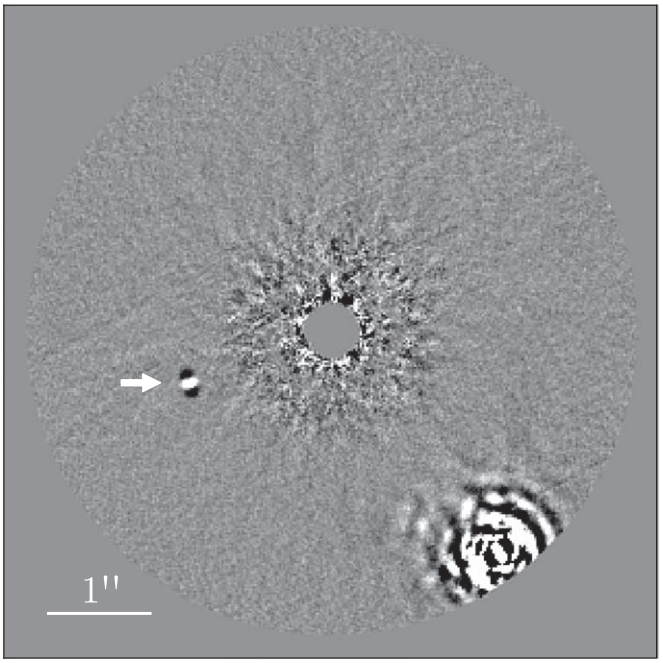

Figure 5. A newly discovered component in the δ Cyg (HIP 97165) system (indicated with an arrow). North is up and east is left. The object near the southwest edge of our field of view is δ Cyg B.

5.1.1. HIP 21547 (51 Eri)

We observed HIP 21547 in 2013 December and in 2015 January. The 2013 data set was not as sensitive as the 2015 data set because they were taken during worse conditions (1.″3 seeing in 2013 compared to 0.″9 in 2015). Our 2015 data were collected with good seeing, include 75 minutes of exposure time, and 34° of rotation. The target, also known as 51 Eri, has a directly imaged planet at 0.″45 separation with an L' contrast of 11.58 (Macintosh et al. 2015; Rajan et al. 2017). Ten percent of our contrast curves attain at least this depth at 0.″45.

We recovered the planet reported by Macintosh et al. (2015) at only 2.4σ in our 2015 data set. The low significance of our detection is likely the result of multiple factors. For one, temporary trouble with the right-side AO system meant this target was observed in single-sided mode, even though most targets were observed in double-sided mode on the same night. Second, the observing log reports variable thin clouds which likely affected the thermal–infrared transmission and background flux level. Lastly, we obtained only 34° of sky rotation, which corresponds to less than 3(λ/D) motion at the separation of the planet and is inadequate for obtaining the deepest contrasts. Analysis of our observing metadata for the survey revealed that our best contrast interior to 0.″7 occurs when we obtain $\gtrsim$70° of rotation.

5.1.2. New Component in the HIP 97165 (δ Cyg) System

We discovered a bright source in our L' imaging data at a position angle of 110° ± 1°.5 separated by 1.″49 ± 0.″04 from the primary in the δ Cyg system, shown in Figure 5. We observed the object in additional infrared filters to characterize its color. We compared our photometry of this newly discovered object (listed in Table 5) to the Baraffe et al. (2015) evolutionary models to estimate its mass, ~0.13–0.2 $M_{\odot}$. The L' photometry of the newly discovered star was measured by injecting a scaled negative image of the unsaturated primary into each of the individual images before performing the PCA analysis. For the *H*, *Ks*, and *Ls* photometry, we measured the brightness of the object using the secondary as a PSF model and PSF fitting after subtracting a 180° rotated version of the image to remove the rotationally symmetric portion of the primary star PSF. All photometric errors are estimated by repeating our measurements several times with a random selection of the data frames (i.e., bootstrapping; see Press et al. 2002).

Table 5
New δ Cyg Companion Photometry

Filter	Abs. mag
L'	8.58 ± 0.06
Ls	8.63 ± 0.12
Ks	8.43 ± 0.05
H	8.38 ± 0.05

While the mass estimates from each band overlap, our photometry suggests a bluer color than predicted by the models. However, systematic differences in the data collection and analysis between the *H*, *Ks*, and *Ls* band images and the L' image complicate our ability to interpret the color.

The δ Cyg system has high proper motion, $pm_{\rm R.A.} = 38 \pm 1.4$ mas yr^{-1}, $pm_{\rm Decl.} = 52 \pm 1.3$ mas yr^{-1} (Gaia Collaboration et al. 2018), but we were not able to confirm common proper motion of the companion with our data. We checked for a similarly bright object in the vicinity of the star in the 2MASS Survey Atlas image taken in 1998. From 1998 to 2015, ~1″ of motion is expected. However, the 2MASS images are saturated out to a radius of ~2.″5, making this test impossible. We also checked observatory archives for other high-contrast imagers, looking for previous observations of δ Cyg. We found none.

We calculate the probability of a chance alignment using the sky density of similarly bright sources in the neighborhood of δ Cyg from the 2MASS Point Source Catalog (Cutri et al. 2003; Skrutskie et al. 2006). For a 10° × 10° patch of sky centered on δ Cyg, the average number of sources with Ks mag less than 12 in a square degree is 631. The implied number of sources within a 1.″5 radius circle is 3.4×10^{-4}.

Assuming all our targets sample a similarly populated portion of the sky, then we expect to have a ~3% chance of detecting an $m_{Ks} = 12$ or brighter source within 1.″5 of one of our 98 stars. However, some of our stars are located in more sparsely populated regions, and some of our stars are located in more densely populated regions of the sky so our derived number, ~3%, should be interpreted with caution. Additional observations of this object are warranted to confidently determine its nature.

5.1.3. Confirmed Background Objects

Our survey is less susceptible to ambiguous background sources than other surveys performed at shorter wavelengths because the much brighter sky background at L' limits the volume of the galaxy we probe with each data set. Yet, we find background objects in the vicinity of three of our targets, HIP 93747 and HIP 92161, which are both at low galactic latitude, and HIP 62512. We compared the LEECH-measured positions of each object to archival Keck NIRC2 data that we reduced to confirm their background nature. Figure 6 shows the relative astrometry for each object compared to the motion expected of a distant background source. We use conservative astrometric error bars based on the analysis of Bowler et al. (2015)

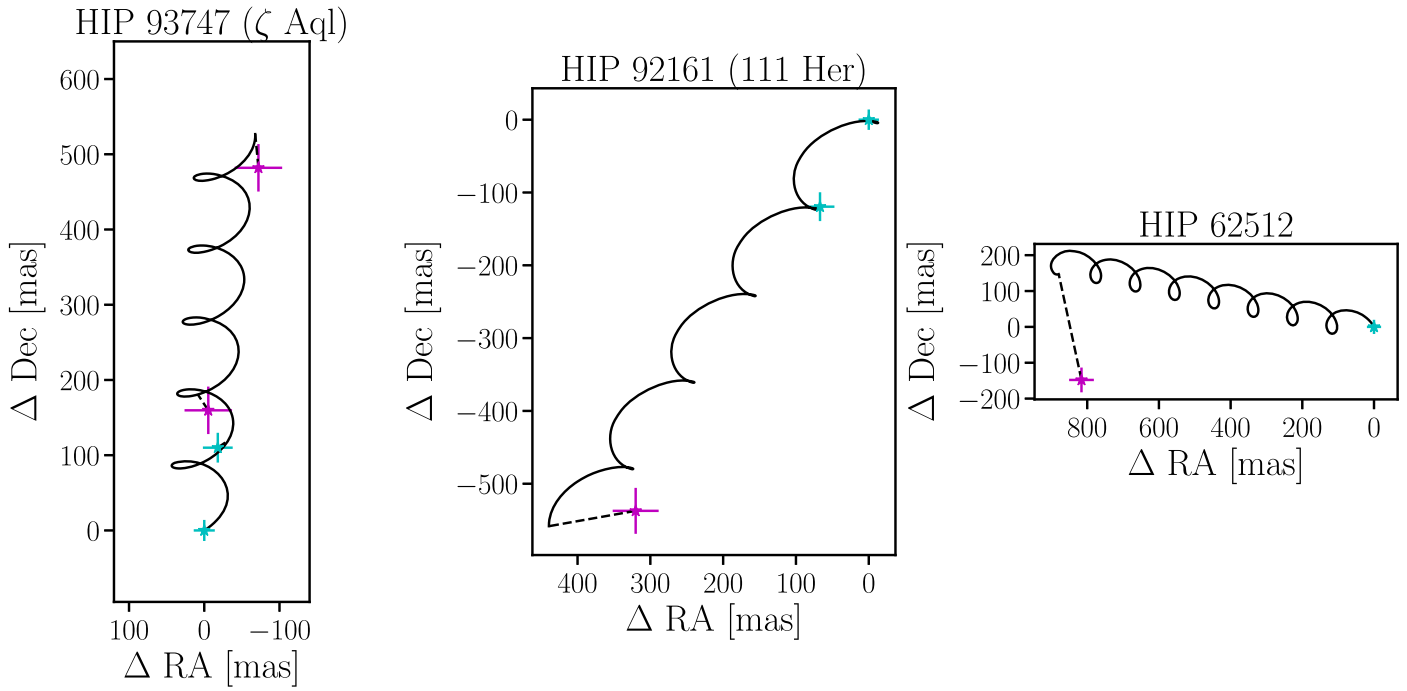

Figure 6. Relative astrometry of faint sources in the vicinity of three of our target stars. Cyan points are from archival NIRC2 data and magenta points are from LMIRcam. Solid curves show the expected motion of stationary background objects with respect to the target star including both proper motion and annual parallax. Dashed lines connect measured astrometric points to the corresponding position of the background track at the time observed. The LEECH point for HIP 62512 is inconsistent with the background track and with Keplerian motion from a bound orbit. We attribute its offset to low signal-to-noise ratio in the NIRC2 data and working close to the edge of the field of view in the LEECH data.

for NIRC2 and Maire et al. (2015) for LMIRcam. Our LMIRcam astrometry includes an additional error of 1 pixel to account for challenges in centroiding the heavily saturated PSFs of the primary stars. The astrometry of the source in the vicinity of HIP 62512 seems inconsistent with the background track presented in Figure 6. The motion of the HIP 62512 source is inconsistent with a bound Keplerian orbit because the minimum average velocity implied by the apparent projected motion from 2005 to 2013 exceeds the maximum escape velocity calculated by assuming the true separation is equal to the projected separation by a factor of ∼3. Thus, we attribute the discrepancy with the background track for this source to systematic errors because the source was imaged at the edge of our field of view in the LEECH data and is also affected by a diffraction spike in the NIRC2 data. Additional observations of this system are warranted to definitively confirm its nature.

5.2. Survey Sensitivity

5.2.1. Photometric Limits

We present two versions of our contrast curves: (1) a "classical" set, which do not correct for small number statistics, and (2) a "modern" set that does include a correction for small number statistics (Mawet et al. 2014). Our "modern" contrast curves indicate a constant number of expected false positives as a function of separation (Jensen-Clem et al. 2018) and ensure 95% completeness. Our varying threshold allows a total of 0.01 false detections within 3″ from our targets. The "classical" contrast curves (described in Section 4) are presented and analyzed for comparison to previous studies. We describe how we adjust these to produce our modern contrast curves in the Appendix. On average, our more carefully constructed modern contrast curves are 0.28 mag less sensitive than our classical curves, though this varies with separation (see the Appendix).

In the left panel of Figure 1, we show the best and median contrast curves from our survey and compare them to the best and median contrast curves from the Rameau et al. (2013) survey, which was also conducted at L'. Comparing like to like, our median classical 5σ contrast is ∼1 mag deeper across the whole range of angular separations probed compared to Rameau et al. (2013). Our best contrast curve is similar to the best curve reported by Rameau et al. (2013). In the right panel of Figure 1, we show median contrast versus projected physical separation assuming a distance equal to the respective survey median target distances. In this case, the performance difference is more pronounced, revealing more than 3 mag of increased contrast interior to 12 au projected separation.

5.2.2. Sensitivity in the Mass–Semimajor Axis Plane

While median contrast curves can provide a good metric for comparing photometric and AO performance, it does not indicate sensitivity to planets. This is because the stellar age and magnitude for each target must be taken into account to convert contrast to limiting magnitude and limiting magnitude to an upper limit on planetary mass with the assistance of an evolutionary model.

Evolutionary models predict how planets of different masses cool and fade over time. We choose to use three different models to derive three separate estimates of our sensitivity to gas-giant exoplanets. These models are DUSTY (Chabrier et al. 2000), COND (Baraffe et al. 2003), and the models presented by Fortney et al. (2008), which we will refer to as F08. Each of the three evolutionary models is built on a different set of extreme assumptions for formation, evolution, and the

atmospheric appearance of substellar objects. None of the models seem to be precise fits to the observed directly imaged planet population, but taken together, they bracket the data in color–magnitude space.

The DUSTY and COND models are both "hot-start" in the sense that they make use of arbitrarily large adiabatic spheres that undergo homologous collapse as their initial condition. These models produce bright young objects (Baraffe et al. 2002; Marley et al. 2007). More physically motivated models for the early evolution of gas-giant luminosities are based on the core-accretion scenario (e.g., Marley et al. 2007; Mordasini 2013). These models can produce a variety of initial post-accretion luminosities depending on the radiative efficiency of the accretion shock while envelope material is being built up (e.g., Mordasini et al. 2017). The core-accretion formation prescription included in the F08 models (that of Hubickyj et al. 2005) appears to produce very-low luminosity young planets (Berardo et al. 2017), so we take our F08 sensitivity to be conservative.

The DUSTY and COND models represent atmospheric extremes with respect to dust and cloud opacity. DUSTY atmospheres exhibit maximal dust opacity, retaining in the photosphere all the dust and condensates that form. COND models assume no photospheric dust opacity, but assume that dust forms and immediately precipitates below the photosphere (taking its constituent molecular species with it). The F08 cold-start models are cloud-free.

Model fits to photometric and spectroscopic measurements of the HR 8799 planets and other young low-gravity gas giants reveal that planets can loft clouds even at effective temperatures where higher-gravity brown dwarfs appear mostly cloud-free (down to ∼900 K; e.g., Barman et al. 2011; Ingraham et al. 2014; Skemer et al. 2014b; Bonnefoy et al. 2016; Currie et al. 2011). Unfortunately, the cloud-containing DUSTY models do not extend to the intermediate ages of all of our targets. The DUSTY models truncate earlier for lower-mass objects (e.g., 40 Myr for 2 $M_{\rm Jup}$, 300 Myr for 6 $M_{\rm Jup}$, 1000 Myr for 10 $M_{\rm Jup}$). In order to better capture the dusty faint appendix to the L-dwarf sequence seen for low-gravity atmospheres (e.g., Liu et al. 2016), we extrapolated the DUSTY models by enforcing that they remain parallel to the COND models but with the same offset as measured for the last age at which both models include predictions. We caution that for the coolest objects, this extrapolation becomes a very poor approximation to the observed flux. The atmosphere of 51 Eri b ($T_{\rm eff} \sim 700$ K) appears to be significantly less cloudy than hotter low-gravity objects, so the cloudy extension to low gravity does not continue to temperatures below ∼700 K (although some cloudiness is necessary to account for the observed L' flux of 51 Eri, these are likely not the silicate clouds modeled in the DUSTY grid; Macintosh et al. 2015; Rajan et al. 2017; Samland et al. 2017). Thus, our extrapolation of the DUSTY models is highly suspect at lower masses. The accuracy of all the evolutionary models we use is limited by the incomplete treatment of the relevant physics—including the initial entropy, the behavior and appearance of clouds, and the treatment of atmospheric dynamics and disequilibrium chemistry—and all of these issues tend to become more severe at lower masses and effective temperatures. Concerning just atmospheric cloudiness, DUSTY models are probably more appropriate than the COND models for hotter planets, while the COND models are more appropriate for cooler planets.

Gas-giant exoplanets are observed to have high mean metal content (Thorngren et al. 2016), and this manifests, at least partially, in metal-enhanced atmospheres (Wong et al. 2004; Skemer et al. 2016; Samland et al. 2017). The evolutionary models we use make different assumptions about the composition of gas-giant planet atmospheres. The Fortney et al. (2008) models are five times solar metallicity, while both the DUSTY and COND models are solar abundance. All three models assume equilibrium atmospheric chemistry, which is not well supported by observations (e.g., Hinz et al. 2010; Barman et al. 2011; Skemer et al. 2012). Fortney et al. (2008) experiment with disequilibrium chemistry in their models, which show a dramatic increase in the emission at L' for atmospheres with effective temperature greater than 500 K due to the reduction of methane opacity when mixing within the photosphere delivers carbon monoxide at a rate faster than chemical reaction timescales (Hubeny & Burrows 2007). This effect is not included in the F08 evolutionary models that we make use of here.

For the evolutionary model (j) and target star (i), we produce a sensitivity map, $s_{ij}(a, m)$, that quantifies our ability to detect planets as a function of orbital semimajor axis, a, and planet mass m. To produce these maps, we use the MESS code (Bonavita et al. 2012). Briefly, MESS performs Monte Carlo injections and takes $s_i(a, m)$ to be the fraction of planets of mass m on randomly oriented Keplerian orbits with semimajor axis a that could be detected around star i with our data. MESS uses evolutionary models to convert m to an apparent L' brightness given the system age and distance and then registers a detection if the L' brightness is detectable at the projected separation given our contrast curve. For this purpose, we generally used our modern contrast curves. We used classical contrast curves only for the purposes of comparing to previous studies.

MESS treats binary stars differently than single stars, respecting dynamical constraints on the position of planets following Holman & Wiegert (1999). Twenty-six binaries are indicated in Table 2, and binary system parameters are summarized in Table 6. We list the critical semimajor axis for circumstellar and circumbinary planets in each system. Circumstellar planets are only allowed interior to $a_{\rm crit}^{\rm cs}$ and circumbinary planets are only allowed exterior to $a_{\rm crit}^{\rm cb}$. The binary mass ratio, orbital semimajor axis, and eccentricity are all required to derive $a_{\rm crit}$. For this purpose, we glean orbital parameters from the Ninth Catalog of Spectroscopic Binary Orbits[23] and the Washington Double Star Catalog.[24] When information on the flux of the secondary star is available, we derive the secondary mass in the same way as for the primaries. When there is no information about the mass of the secondary, we assume a mass ratio of 1. This is the most conservative assumption because it maximizes the excluded parameter space. When binary semimajor axis information is missing, we derive the value using the system period and component masses. When the binary eccentricity is unavailable, we assume a value of 0.5, following Bonavita et al. (2016).

In total, 19 out of 26 binaries in the LEECH survey have some portion of the 1–500 au range of orbital semimajor axes explored by MESS excluded. The remaining systems consist of such close binaries that the critical radius is within 1 au. Because dynamics excludes the existence of planets at some positions, we emphasized targeting binaries during intervals of poor observing conditions to minimize the impact of relatively poor AO performance.

In Figure 7, we show examples of the MESS output for each evolutionary model using our modern contrast curves. Both the mean sensitivity map averaged over all targets and an example

[23] http://sb9.astro.ulb.ac.be/
[24] http://ad.usno.navy.mil/wds

Table 6
Summary of Binary System Parameters

Name	M1 [$M_\odot$]	M2 [$M_\odot$]	M2/M1[a]	Sep. [″]	ecc.	$a_{\rm crit}^{\rm cs}$ [b] (au)	$a_{\rm crit}^{\rm cb}$ [c] (au)	Note
HIP 8486[d]	1.05	⋯	1	0.53	0.45	⋯	44.5	
HIP 8832[d]	2.17	2.7	1	8	⋯	109.7	972.0	
HIP 8903[d]	2.08	1.2	0.57	⋯	⋯	⋯	1.6	
HIP 10064[d]	2.39	⋯	1	0.01	0.44	⋯	1.1	
HIP 10552[d]	0.85	0.75	0.88	0.35	0.59	⋯	48.0	
HIP 12828[d]	1.73	⋯	1	⋯	⋯	⋯	4.5	1202.2 day period
HIP 14576	3.48	1.70	0.48	⋯	0.26	⋯	8.7	$a_{\rm crit}$ from Bonavita et al. (2016)
HIP 25486[d]	1.06	0.76	0.71	⋯	⋯	⋯	10.0	$a_{\rm crit}$ from Bonavita et al. (2016)
HIP 27913[d]	1.1	⋯	1	0.09	0.45	⋯	11.0	
HIP 28360	2.79	⋯	1	0.003	0.0	⋯	0.2	
HIP 41820[d]	1.00	0.75	0.75	0.41	0.71	⋯	45.9	
HIP 44458[d]	1.11	0.56	0.50	1.72	⋯	17.4	126.3	
HIP 49669	3.4	0.3	0.09	⋯	0	⋯	0.7	$a_{\rm crit}$ from Bonavita et al. (2016)
HIP 58001[d]	2.62	1.25	0.48	0.46	0.3	⋯	52.8	
HIP 62512[d]	1.3	⋯	1	0.04	0.14	⋯	3.3	
HIP 63503[d]	1.55	0.90	0.58	1.21	0.39	5.9	106.9	
HIP 65378[d]	2.67	0.5	0.19	0.78	0.6	⋯	82.8	
HIP 72603[d]	1.4	0.9	0.64	0.4	⋯	⋯	23.0	
HIP 72659[d]	1	0.7	0.7	4.94	0.51	⋯	126.3	
HIP 72848	0.9	⋯	1	0.02	0.51	⋯	0.7	
HIP 76267	2.58	0.92	0.35	⋯	0.37	⋯	0.7	$a_{\rm crit}$ from Bonavita et al. (2016)
HIP 83207	2.91	⋯	1	⋯	⋯	⋯	0.1	4.02 day period
HIP 85829	1.62	⋯	1	⋯	⋯	⋯	0.48	38.1 day period
HIP 86032[d]	2.10	1.16	0.55	0.43	0.92	⋯	27.73	
HIP 97165[d]	3.14	1.55	0.49	3.41	0.52	23.4	678.8	
HIP 107556	1.5	0.56	0.37	⋯	0.1	⋯	0.06	$a_{\rm crit}$ from Bonavita et al. (2016)

Notes.
[a] We conservatively assume a mass ratio of 1 when there is no constraint on the secondary mass. This maximizes the excluded parameter space.
[b] The circumstellar critical radius. Planets are dynamically excluded on orbits with larger semimajor axes, following Holman & Wiegert (1999).
[c] The circumbinary critical radius. Planets are dynamically excluded on orbits with smaller semimajor axes, following Holman & Wiegert (1999).
[d] These targets include some restricted parameter space in the LEECH sensitivity maps.

of a sensitivity map for a specific target are shown. The number of targets used to make the average maps is indicated in each panel. For the F08 models, we were only sensitive to planets around 12 of our stars, so we only average those targets. The hashed region of the F08 panels in Figure 7 indicates the portion of parameter space that we did not explore with MESS.

As expected, we are more sensitive to hot-start planets like those modeled in the DUSTY and COND grids. Of the two, we are most sensitive to DUSTY planets, since these objects emit a greater fraction of their luminosity in the L'-band because cloud opacity in the photosphere pushes the emission spectrum to longer wavelengths.

The peak of our mean sensitivity is centered between ∼30 and ∼50 au, but as suggested in Figure 7, the range of semimajor axes probed is different for each star and depends on the distance. Indeed, our mean maps indicate significant ($\gtrsim$10%) sensitivity to companions $\lesssim 20\,M_{\rm Jup}$ extending in to ∼5 au.

6. Statistical Analysis

We use LEECH sensitivity maps to derive statistical constraints on the gas-giant planet occurrence frequency at wide separations.

We did not discover any new planets with the LEECH survey, but as we will show, we can use our unique sensitivity to place the best-yet limits on cold-start planets interior to 20 au around FGK stars. We also show improved sensitivity to hot-start planets interior to ∼10–20 au compared to many previous surveys.

Following the statistical formalism of Lafrenière et al. (2007a), for zero new discoveries d, we adopt the likelihood function

$$L(d = 0|f) = \prod_i^N (1 - f s_i), \tag{5}$$

which takes the probability of detecting a planet around the ith star to be the planet occurrence frequency, f, times our measurement sensitivity determined for that target s_i. With the likelihood function in Equation (5), we can calculate a posterior distribution using Bayes theorem,

$$p(f|d = 0) = \frac{L(d = 0|f)p(f)}{\int_0^1 L(d = 0|f)p(f)df}, \tag{6}$$

where $p(f)$ is the prior probability distribution for f. The posterior distribution $p(f|d = 0)$ places an upper limit on the planet occurrence frequency at a given level of confidence, CL,

$$\mathrm{CL} = \int_0^{f_{\rm max}} p(f|d = 0)df. \tag{7}$$

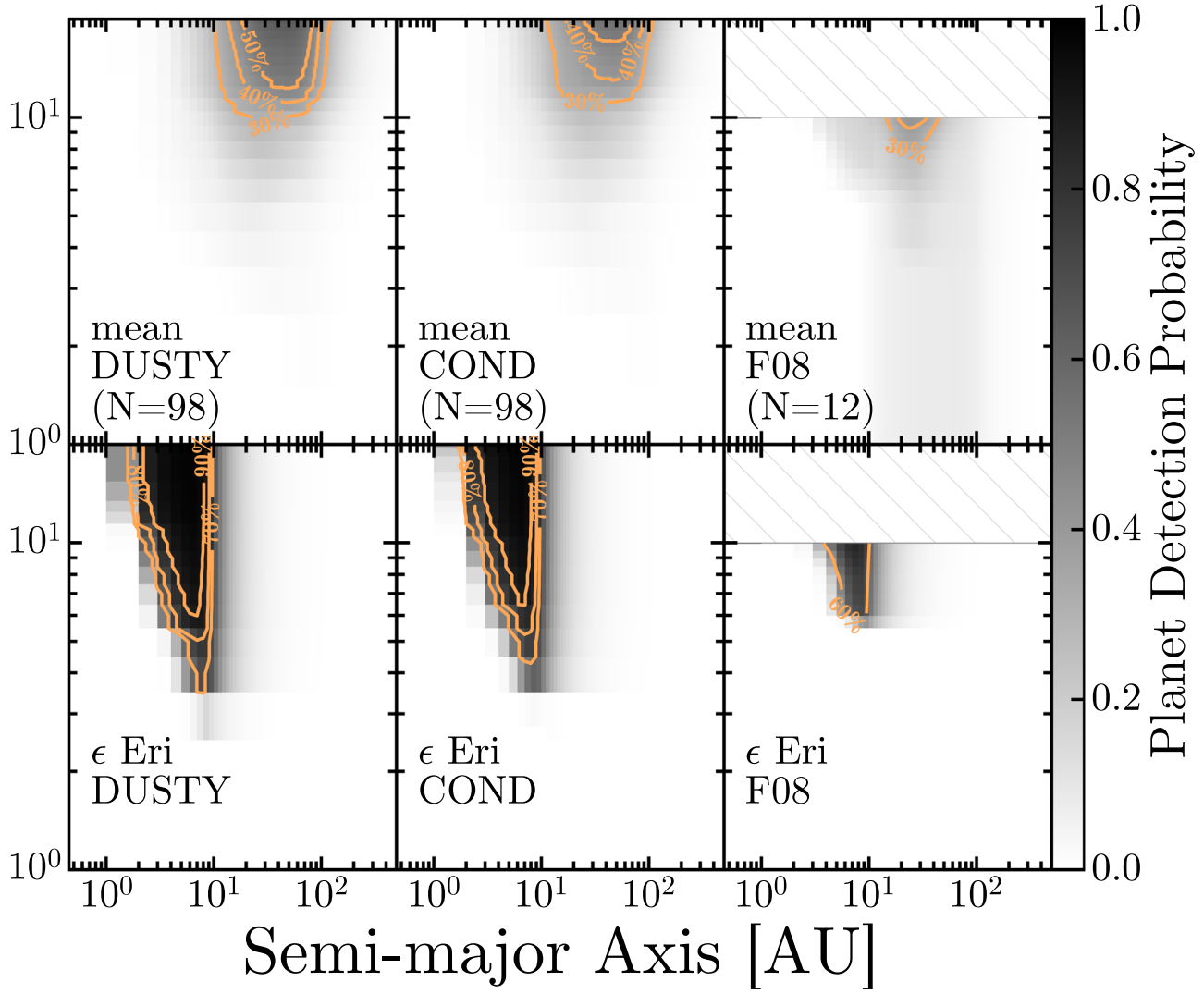

Figure 7. Sensitivity maps showing planet detection probability as quantified using MESS (grayscale and contours). The evolutionary model used is indicated in each panel. The F08 models do not extend above 10 $M_{\rm Jup}$. Top row: the mean sensitivity maps averaged over all targets. The number of targets contributing to the mean is indicated. Since we were only sensitive to cold-start planets around 12 stars, the number of targets used to create the mean F08 map is 12. Bottom row: Sensitivity maps for ϵ Eri.

6.1. Mapping Occurrence Frequency in the Mass–Semimajor Axis Plane

For each of our sets of sensitivity maps—corresponding to the three different evolutionary models we used—we create maps that show our 95% confidence upper limit to the planet frequency. That is, for each point (a, m) in our grid, with a the semimajor axis and m the planet mass, we calculate a likelihood function according to Equation (5), substituting $s_i(a, m)$ for s_i. Then, we use Equations (6) and (7) to derive our 95% confidence limit on the planet occurrence frequency. For this purpose, we assume a uniform prior similar to other studies (e.g., Lafrenière et al. 2007a).

The results for each evolutionary model are shown in Figures 8–10 (DUSTY, COND, and F08, respectively). For the DUSTY and COND constraints, in addition to performing the analysis on the total LEECH sample, we divided the targets into subgroups of interest. These subgroups include the subset of single stars, the subset of FGK stars, the subset of A- and B-type stars, the subset of A and F stars with evidence of circumstellar dust, and the subset of stars that are members of the Ursa Major moving group. While some of these subgroups resemble our target selection sublists, not all of them correspond directly and some targets are members of multiple subgroups. For example, all of the dusty A stars are included in our AB subgroup, and all FGK stars in the UMa sublist are also included in our FGK subgroup, etc. The reordering of objects into slightly different subgroups compared to the the target selection sublists described in Section 2 was necessary because we did not complete observations for all our targets, and because our dynamic nightly scheduling resulted in uneven completion of the sublists.

Our cold-start subgroup is made up of all the stars for which we had some sensitivity to the planets predicted by the F08 models, given our photometric sensitivity, as well as the system age and distance. This subgroup includes 12 stars. These targets are indicated in Table 2.

6.2. Comparing LEECH Maps to Previous Surveys

The LEECH survey makes its most unique and significant contribution at small separations from FGK-type stars. To show

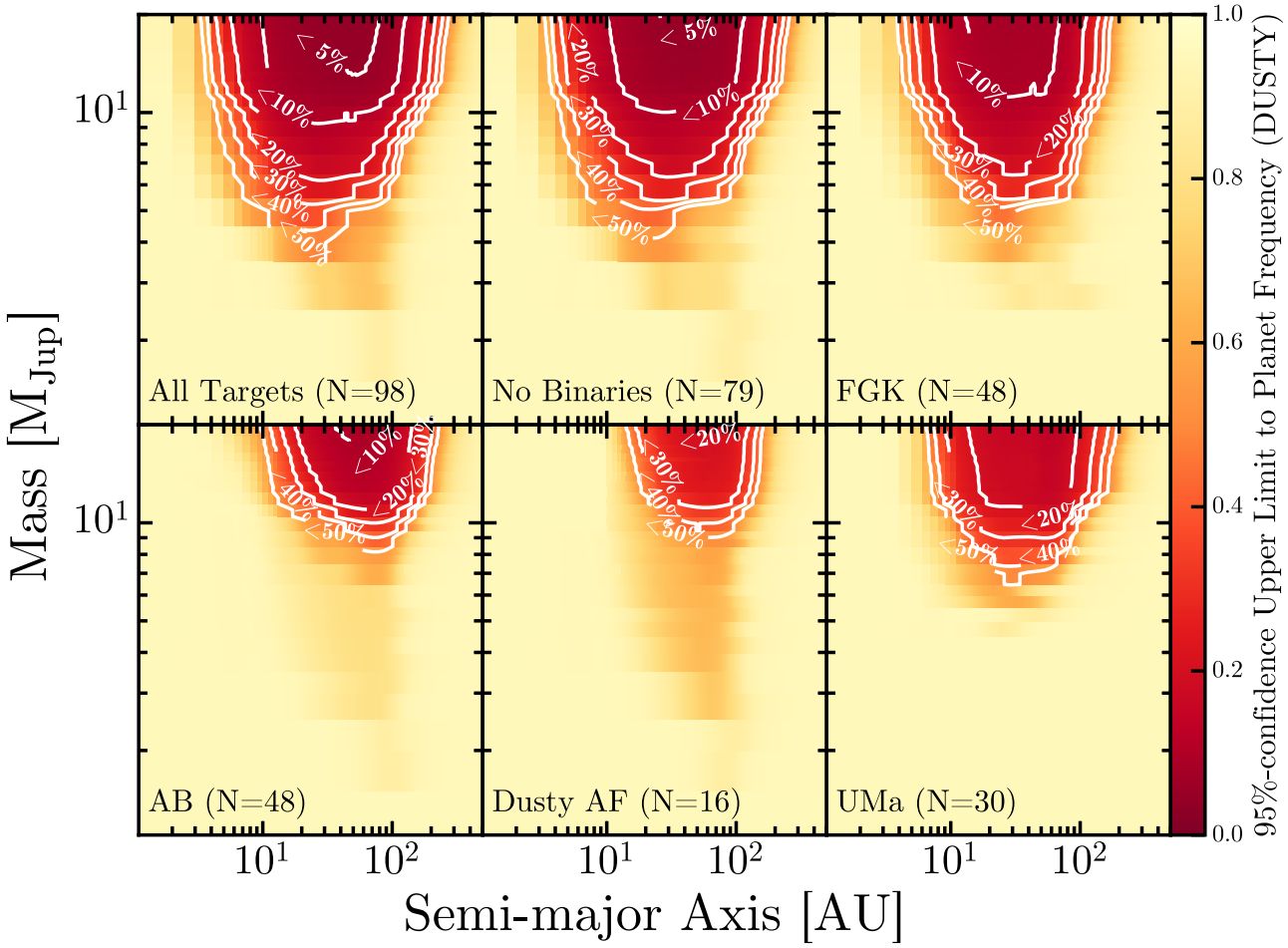

Figure 8. The LEECH 95% confidence upper limits to the planet occurrence frequency over a fine grid in the mass–semimajor axis plane calculated using the DUSTY evolutionary models extrapolated as described in the text (red colorscale and white contours). We subdivide our sample into groups as described in the text.

the new parameter space probed by LEECH, we compare our performance to previous studies. In order to make the comparison as direct as possible, we reanalyze our data using contrast curves created with the classical 5σ approach (not correcting for small number statistics or varying the false-alarm rate with separation). In Figure 11, we show recalculated maps for both COND hot-start evolutionary models and the F08 cold-start models. Our COND map is specific to our FGK subgroup and is made using 54 stars. We overplot the 50% contour from Nielsen & Close (2010), Biller et al. (2013), and Chauvin et al. (2015).[25] LEECH improves constraints on COND-like planet occurrence frequency at small separations ($\lesssim$10–20 au), even though we targeted much older systems whose hot-start planets should be intrinsically much less luminous.

For cold-start planets, only Nielsen & Close (2010) and Brandt et al. (2014) reported limits for FGK-type stars. Nielsen & Close (2010) published an occurrence frequency map, and we compare our LEECH results to theirs in Figure 11. LEECH performs better interior to ~25 au. We discuss the results of Brandt et al. (2014) at more length in Section 7.

In Figure 12, we show our map of upper limits to the planet occurrence frequency for A- and B-type stars made with classical 5σ contrast curves. We overplot the 50% contour of a similar map from Nielsen et al. (2013). In this case, the LEECH 50% contour is always within the Nielsen et al. (2013) contour, so we do not improve constraints on the planet occurrence frequency compared to Nielsen et al. (2013). However, as discussed in Section 2, we used a different set of model isochrones than Nielsen et al. (2013) when estimating the ages of our A- and B-type targets, and our age estimates are typically two times as large as those found by Nielsen et al. (2013). This will make LEECH appear less sensitive to planets around these types of stars.

Many of our UMa targets were also observed by Ammler-von Eiff et al. (2016) as part of the *K*-band coronagraphic imaging survey. While Ammler-von Eiff et al. (2016) considered group ages spanning 100–1000 Myr, they report mean sensitivity $\lesssim$5% to 20 $M_{\rm Jup}$ COND-like objects assuming a group age of 500 Myr. LEECH delivers 30% mean sensitivity to 10 $M_{\rm Jup}$ objects.

We note that there are some compilation studies that perform statistical analysis on large target lists using as input contrast curves from multiple studies (e.g., Brandt et al. 2014; Bowler 2016; Galicher et al. 2016). We cannot compare directly to those studies in Figures 11 and 12 because they do not provide

[25] Our approach used the same definition for contrast curves as used in Nielsen & Close (2010) and Chauvin et al. (2015). The comparison to the Biller et al. (2013) contour is not as direct, since those authors defined their contrast curves with a higher true-positive rate (see, for example, Jensen-Clem et al. 2018, for a review of the signal detection terminology). However, when we compare the Biller et al. (2013) 50% contour to the FGK map in Figure 9, which is based on our more rigorous contrast curves, we still provide better constraints at small separation.

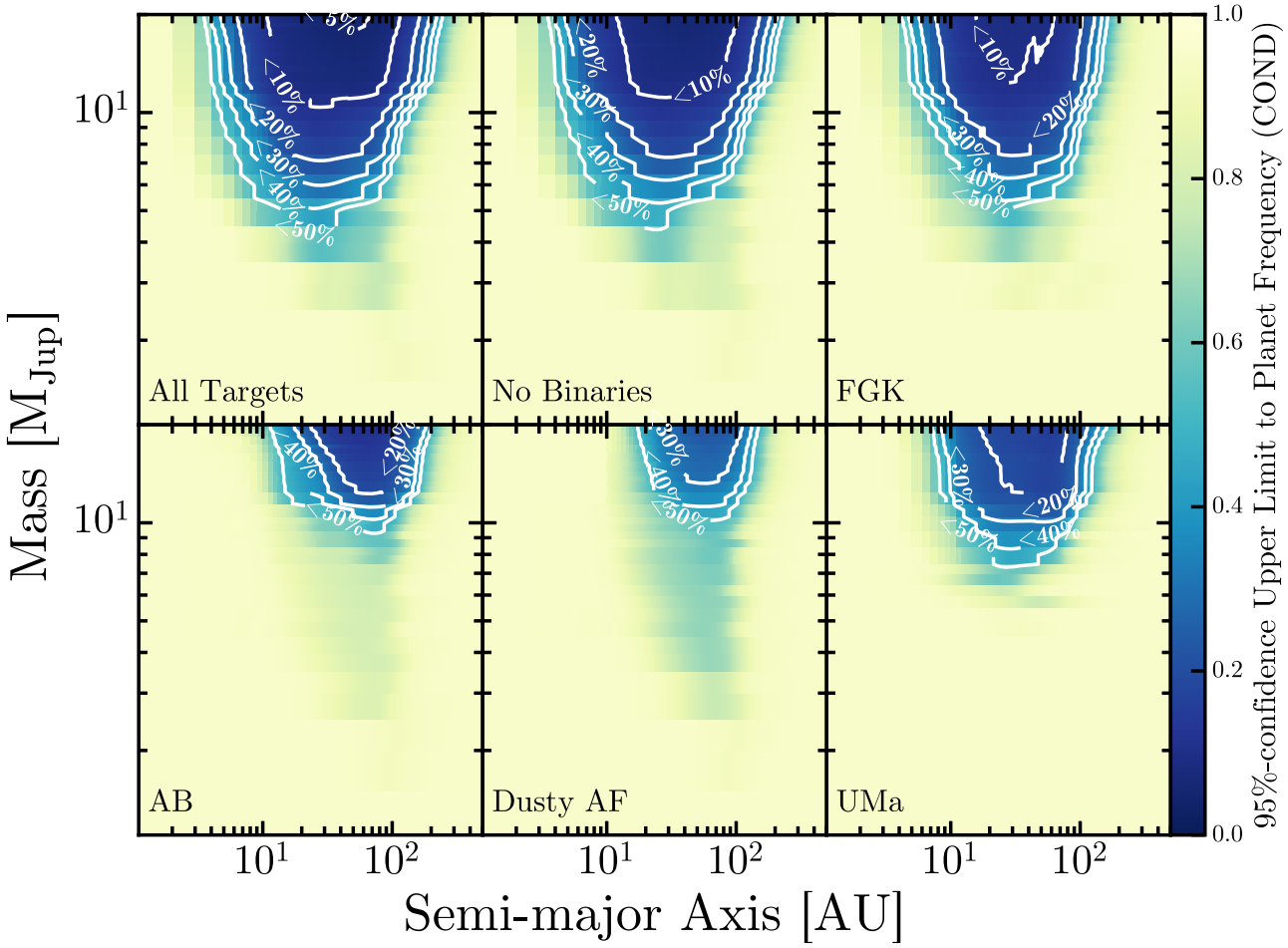

Figure 9. The LEECH 95% confidence upper limits to the planet occurrence frequency over a fine grid in the mass–semimajor axis plane calculated using the COND evolutionary models (blue colorscale and white contours). We subdivide our sample into groups as described in the text.

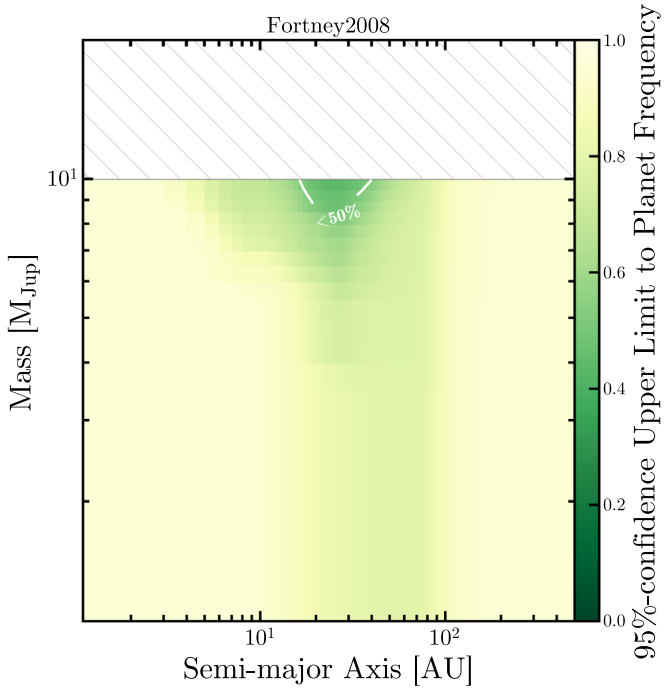

Figure 10. LEECH 95% confidence upper limits to the planet occurrence frequency over a fine grid in the mass–semimajor axis plane calculated using the F08 cold-start evolutionary models. We are sensitive to cold-start planets around 12 of our targets.

a similar occurrence map. However, published compilation analyses typically provide much stronger constraints than we show because they use a much larger number of stars. We will discuss their results in comparison to LEECH in Section 7. Figure 11 suggests LEECH contrast curves will improve planet frequency constraints on solar system scales in future compilation studies.

6.3. Occurrence Frequency for Ranges of Mass and Separation

To place an upper limit on the occurrence frequency of planets within a range of masses and separations, we again make use of Equations (5)–(7), but now we define our sensitivity to planets for each star, s_i, to be the fraction of all Monte Carlo injected planets over the whole range that we would detect with our LEECH data.

Figure 7 illustrates that we are more likely to detect companions in certain regions of parameter space than others. Thus, a single constraint on the planet frequency over a wide range in parameter space will depend on our assumed shape of the underlying planet distribution. For example, if we assume there should be lots of planets where we have a good chance of detecting them, then we can put a better constraint on the occurrence frequency than if we assume most planets are in regions where we are unlikely to detect them.

For a population of planets assumed to be uniform over our grid, our sensitivity over a range of masses and semimajor axes

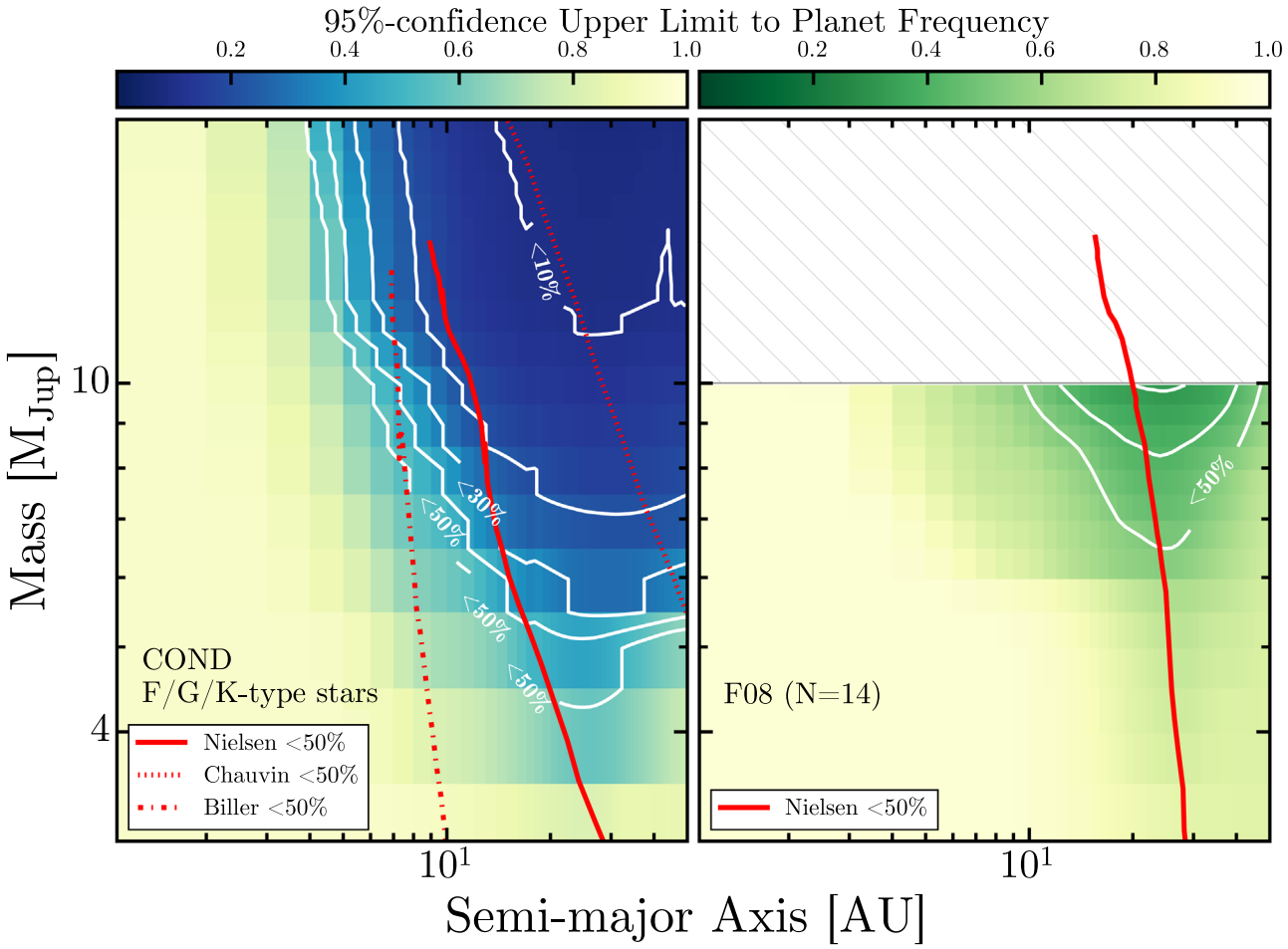

Figure 11. Constraints rederived with classical 5σ contrast curves for comparison to earlier surveys. Left: LEECH 95% confidence upper limits to planet frequency around FGK stars as a function of orbital semimajor axis and planet mass using COND evolutionary models and our classical 5σ contrast curves, blue color map, and white contours. We overplot, in red, the 50% upper-limit contour from three other surveys that publish similar maps for target lists with similar spectral-type distributions (Nielsen & Close 2010; Biller et al. 2013; Chauvin et al. 2015). LEECH provides the best constraints at small semimajor axes. Right: same as for the left panel but for the F08 models. Here we compare to Nielsen & Close (2010), who reported results for a similar spectral-type distribution mainly consisting of FGK stars. LEECH provides the best constraints on cold-start planets interior to ~20 au.

is simply the average sensitivity in that range. For a non-uniform underlying planet distribution, our sensitivity over a range of masses and separations must be calculated using a weighted average over our sensitivity grids—essentially scaling the number of injected planets at each grid point as if the original Monte Carlo analysis was performed using the assumed shape of the planet frequency distribution (e.g., Kasper et al. 2007). That is, we take the sensitivity to planets with masses from $m_{\rm min}$ to $m_{\rm max}$ and semimajor axes from $a_{\rm min}$ to $a_{\rm max}$ to be

$$s_{i,\rm range} = \frac{\sum_{m_{\rm min}}^{m_{\rm max}} \sum_{a_{\rm min}}^{a_{\rm max}} w(a,\, m) s_i(a,\, m)}{\sum_{m_{\rm min}}^{m_{\rm max}} \sum_{a_{\rm min}}^{a_{\rm max}} w(a,\, m)}, \tag{8}$$

where $s_i(a,\, m)$ is the sensitivity map for star i, described in Section 5.2.2, and $w(a,\, m)$ is the weight function that assumes the shape of the underlying planet distribution. Different authors make different assumptions about the shape of the wide-orbit giant-planet distribution in their analyses. For example, Meshkat et al. (2017) assumed a log-uniform distribution, similar to that seen for binary stars in some cases (e.g., Duchêne & Kraus 2013),

$$\frac{\partial^2 f}{\partial \ln a \partial \ln m} \propto m^0 a^0, \tag{9}$$

and Rameau et al. (2013) and Galicher et al. (2016) presented results for a distribution that has the same power-law indices as measured for close-in giant planets (Cumming et al. 2008),

$$\frac{\partial^2 f}{\partial \ln a \partial \ln m} \propto m^{-0.31} a^{0.39}. \tag{10}$$

and for a uniform distribution, which is not physically motivated, but rather the default when sensitivity maps are created with uniform gridding and weights are not used in Equation (8),

$$\frac{\partial^2 f}{\partial \ln a \partial \ln m} \propto m^1 a^1. \tag{11}$$

Some authors have moved beyond the power-law model, particularly for the more well-constrained giant-planet population around M-stars. For example, Meyer et al. (2018) used a log-normal distribution in semimajor axis for planets from 1 to

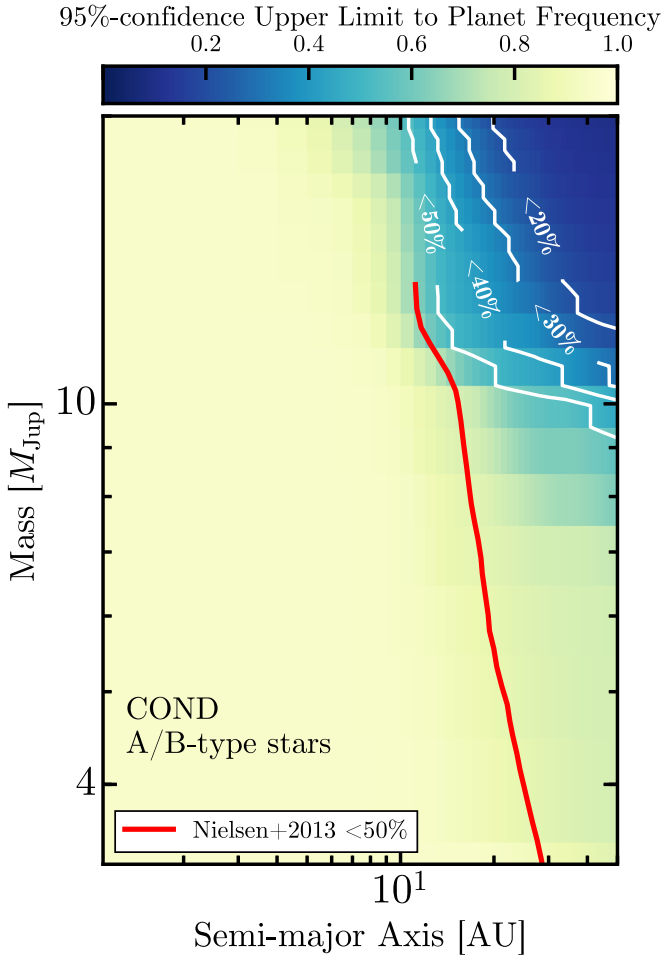

Figure 12. LEECH 95% confidence upper limits to planet frequency around A and B stars as a function of orbital semimajor axis and planet mass using COND evolutionary models and our classical 5σ contrast curves, blue color map, and white contours. We overplot, in red, the 50% upper-limit contour from Nielsen et al. (2013). The LEECH 50% contour is always within the Nielsen et al. (2013) contour, so we do not improve upon their results. However, LEECH typically uses older target ages than the Nielsen et al. (2013), by a factor of 2, reducing our derived sensitivity.

10 $M_{\rm Jup}$,

$$\frac{df}{d\ln a} \propto e^{\left(\frac{\ln a-\mu}{2\sigma^2}\right)}, \tag{12}$$

with μ and σ the mean and variance of the log-normal, respectively.

In Table 7, we show our upper limits to planet frequency for multiple ranges in mass and semimajor axis. For each range, we report results for three different assumed planet distributions: (1) a power law with indices taken to match those derived for close-in giant planets (Cumming et al. 2008), (2) a log-uniform distribution, and (3) a uniform distribution.

7. Discussion

7.1. Planet Frequency Interior to 100 au

It is reasonable to expect that the structure of protoplanetary disks will affect the mass and semimajor axis distributions of giant planets. For example, increased surface density of solids beyond the snow line could easily result in differently shaped planet populations interior and exterior to ~3–5 au. Similarly, beyond the outer radii of protoplanetary disks, we might expect very few planets. Recent, unbiased surveys with ALMA indicate that the dust-disk radii in a typical star-forming region are $\lesssim$40 au with very weak dependence on stellar mass (Eisner et al. 2018). Dust disks in less common, more diffuse star-forming regions are larger, and size correlates more strongly with stellar mass in these environments; however, dust disks rarely extend beyond ~100 au (e.g., Tazzari et al. 2017). Gas disks do extend beyond the observed dust, but only by a factor of ~2 (Ansdell et al. 2018). As a result, constraints on planet occurrence frequency derived assuming distributions that extend well beyond ~100 au are likely underestimated. Furthermore, recent observations of shock-tracing Hα emission from accreting young planets (Sallum et al. 2015; Wagner et al. 2018) suggests that hot-start evolutionary models are overly optimistic in their luminosity predictions. As a result, constraints on planet occurrence frequency derived assuming hot-start models are likely underestimated. More physically meaningful constraints should be derived using cold-start models and semimajor axis ranges better matched to where we expect planets (e.g., interior to outer dust-disk radii).

Given a model for the giant-planet population distribution, our upper limits in Table 7 are effectively constraints on the normalization of the model. That is, for a power-law model,

$$f_{\rm upper} = \int_{a_{\rm min}}^{a_{\rm max}} \int_{m_{\rm min}}^{m_{\rm max}} N a^{\beta} m^{\alpha}\, d\ln m\, d\ln a, \tag{13}$$

with $f_{\rm upper}$, α, and β fixed, we can solve for N, the largest admissible normalization of the distribution allowed by the data.

Figures 13 and 14 graphically depict our upper limits for FGK-type systems. Figure 13 shows our results associated with hot-start models and is specific to planets from 4 to 14 $M_{\rm Jup}$. Figure 14 shows our results associated with the cold-start Fortney et al. (2008) models and applies to the mass range of 7–10 $M_{\rm Jup}$. In both figures, we show $df/d\ln a$ as a function of orbital semimajor axis. Each plot includes colored curves indicating upper limits. Their slopes show the assumed shape of the underlying planet population (Cumming et al. 2008 indices or log-uniform), and their horizontal extent shows the corresponding semimajor axis range used to derive the frequency upper limit. Figures 13 and 14 make it clear that our derived constraints on planet frequency depend sensitively on the evolutionary model used (e.g., hot versus cold) and on the assumed shape of the underlying distribution, including its radial extent.

We highlight two semimajor axis ranges in Figures 13 and 14: 5–50 au, corresponding to the domain of the solar system giants, and 5–100 au, bracketing the orbits of the imaged planets in the HR 8799 system. In each plot and for each power-law slope, using the wider range forces a lower normalization of the population distribution. This is due to the assumption that the underlying shape of the planet population remains fixed throughout the range considered, which means that regions of high sensitivity within the range affect the normalization throughout the range. We provide additional examples of this effect from the literature in the right panel of Figure 13. Bowler (2016) provided an upper limit to 5–13 $M_{\rm Jup}$ planets over two ranges of orbital separation, 10–100 au (<6.8%) and 10–1000 au (<5.8%), assuming a log-uniform distribution of planet masses and orbital semimajor axes for the underlying population. We use the Bowler (2016)

Table 7
95% Upper Limits to Planet Frequency

Subgroup	DUSTY						COND						F08	
	5–50 au			5–100 au			5–50 au			5–100 au			5–50 au	5–100 au
	4–14M_J	8–14M_J	4–20M_J	4–14M_J	8–14M_J	4–20M_J	4–14M_J	8–14M_J	4–20M_J	4–14M_J	8–14M_J	4–20M_J	7–10M_J	7–10M_J
Cumming 2008: $\frac{\partial^2 f}{\partial \ln a \partial \ln m} \propto m^{-0.31} a^{0.39}$														
all	19.7%	11.1%	15.0%	19.7%	10.7%	14.6%	24.7%	13.9%	18.7%	25.3%	13.9%	18.5%	71.4%	75.7%
FGK	26.0%	14.9%	21.0%	27.6%	15.6%	22.1%	31.7%	17.8%	25.0%	33.9%	18.8%	26.3%	87.7%	90.3%
AB	78.7%	52.9%	60.3%	67.2%	38.4%	46.6%	86.1%	72.0%	75.7%	79.3%	57.2%	62.7%	…	…
AF	80.1%	67.7%	73.3%	72.1%	55.1%	62.8%	84.3%	76.8%	79.7%	78.1%	67.3%	70.9%	…	…
UMa	60.0%	31.8%	47.0%	60.5%	30.5%	45.9%	71.2%	39.0%	56.6%	72.6%	38.5%	56.5%	…	…
Log-uniform Distribution: $\frac{\partial^2 f}{\partial \ln a \partial \ln m} \propto m^0 a^0$														
all	20.1%	12.2%	15.1%	19.6%	11.6%	14.3%	25.1%	15.2%	18.7%	25.0%	14.8%	18.0%	73.6%	76.7%
FGK	26.6%	16.2%	21.1%	27.0%	16.4%	21.2%	32.5%	19.5%	25.0%	33.2%	19.7%	25.2%	88.6%	90.1%
AB	81.7%	60.9%	63.2%	72.5%	46.3%	50.0%	87.9%	78.0%	78.3%	83.2%	66.3%	67.1%	…	…
AF	84.3%	75.9%	78.3%	78.2%	64.7%	68.9%	87.5%	82.7%	83.6%	83.2%	75.4%	76.7%	…	…
UMa	60.5%	35.0%	46.6%	59.5%	33.1%	44.6%	71.5%	42.9%	56.0%	71.2%	41.5%	54.5%	…	…
Uniform Distribution: $\frac{\partial^2 f}{\partial \ln a \partial \ln m} \propto m^1 a^1$														
all	12.9%	9.2%	9.0%	13.4%	9.3%	8.9%	16.3%	11.6%	11.2%	17.6%	12.3%	11.3%	67.0%	74.5%
FGK	17.6%	12.8%	13.6%	20.2%	14.6%	15.3%	21.0%	15.0%	15.7%	24.4%	17.4%	17.7%	85.3%	90.7%
AB	54.8%	38.3%	30.8%	41.0%	27.5%	23.2%	72.0%	57.4%	45.4%	58.4%	42.6%	33.4%	…	…
AF	63.8%	53.1%	49.2%	54.4%	42.7%	39.9%	72.1%	64.6%	59.1%	64.1%	55.3%	49.1%	…	…
UMa	38.4%	26.3%	28.1%	39.7%	26.2%	27.6%	47.3%	32.0%	33.3%	50.7%	33.1%	33.9%	…	…

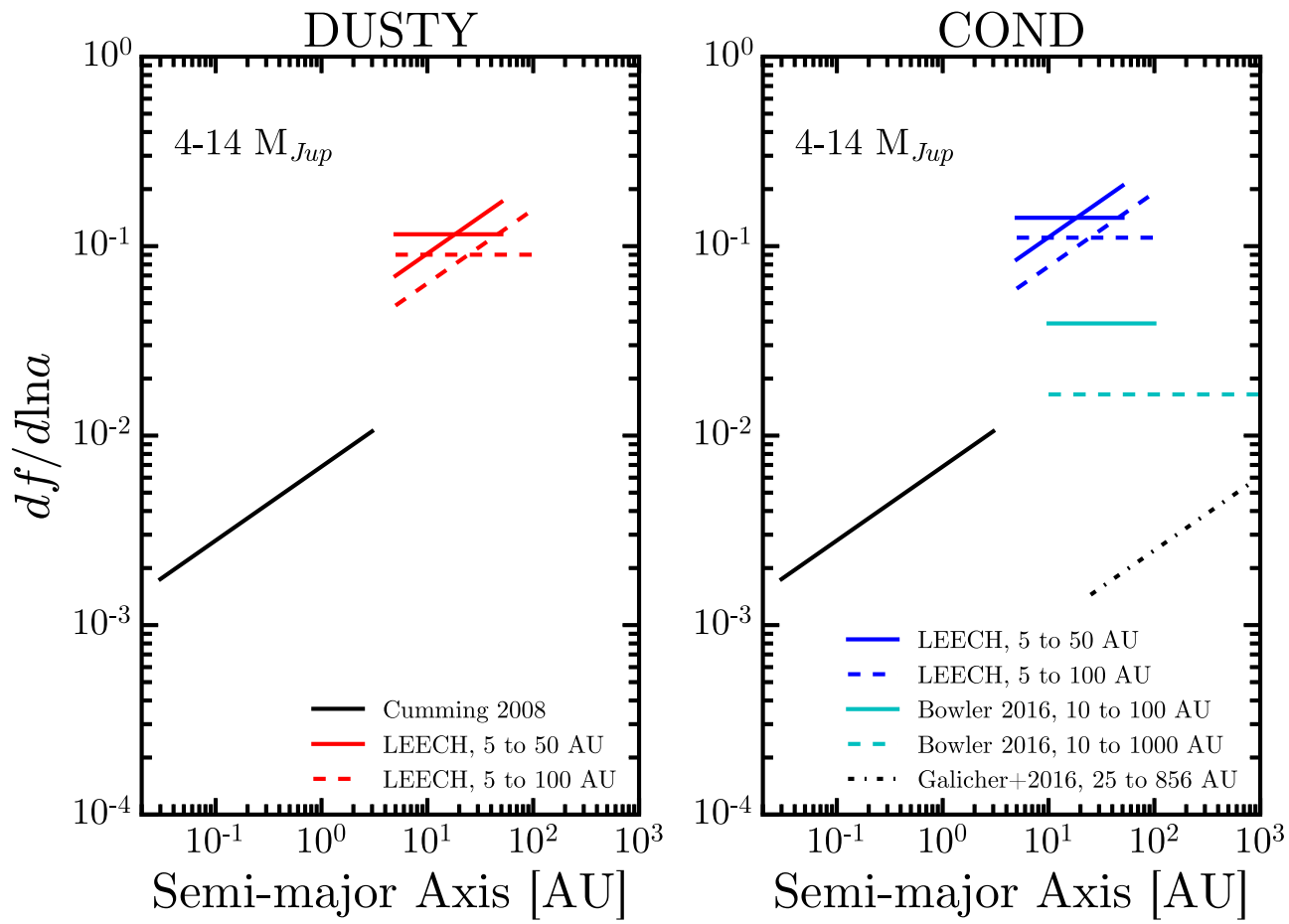

Figure 13. LEECH constraints on power-law planet distributions outside 5 au around FGK stars using hot-start planetary evolution models. All curves assume either a log-uniform semimajor axis distribution of the planet population (horizontal) or a power-law distribution with the same indices as found for the RV planets interior to 3 au but allowing for a different normalization (inclined). Upper limits are shown with colored curves, and best fits are shown in black. We use the LEECH constraints on planet fraction to derive an upper limit to the normalization for an assumed power-law distribution as explained in the text according to Equation (13), and then integrate over masses from 4 to 14 $M_{\rm Jup}$ to yield a function of separation. Left: our constraints specific to the DUSTY hot-start models are shown in red. The solid red curves indicate our constraints using LEECH results from 5 to 50 au, and the dashed curves indicate constraints using LEECH results from 5 to 100 au. Right: LEECH upper limits specific to the COND evolutionary models are shown in blue for the same semimajor axis ranges as the left panel. We also plot, with cyan curves, the upper limits derived by Bowler (2016) using log-uniform distributions from 10 to 100 au (solid) and 10–1000 au (dashed). The reported best-fit distribution for wide-orbit planets from 4 to 14 $M_{\rm Jup}$ and from 25 to 856 au from Galicher et al. (2016) is shown with a black dotted–dashed curve.

results to solve for N in Equation (13) and then adjust the upper limit for the range 4–14 $M_{\rm Jup}$ before plotting the corresponding curves in Figure 13. Once again, the limiting normalization for the population distribution is forced lower when using the wider range. The Bowler (2016) result is based on a compilation of several surveys and includes 155 FGK stars. Compared to LEECH alone (54 FGK stars) the Bowler (2016) compilation constraint is more stringent, however Bowler (2016) does not report limits for the more narrow 5–50 au range, and this is where LEECH makes the greatest contribution.

We also compare to the Galicher et al. (2016) result that 1.1% of FGK stars have a 4–14 $M_{\rm Jup}$ COND-like giant planet in the range from 25 to 856 au assuming a power-law distribution with indices taken from the close-in RV population. The corresponding curve in Figure 13 is inconsistent with an extrapolation of the close-in planet population, implying that some change in the distribution occurs somewhere between 3 and 856 au. Indeed, previous imaging surveys have shown that the shape of the short-period gas-giant distribution cannot be extended beyond ∼60 au (e.g., Kasper et al. 2007; Nielsen & Close 2010; Brandt et al. 2014; Reggiani et al. 2016). While it is not surprising that the planet population is not a single power law from 0.03 to 856 au, it does make it difficult to interpret the 1.1% frequency reported by Galicher et al. (2016). The assumption of a single power law from 25 to 856 au is built into the result. If instead the planet population falls off beyond some radius, then all of the survey sensitivity outside that radius contributes less and less to constraining the normalization of the population (Equation (8)). As a result, a much higher occurrence frequency can be allowed by the data because sensitivity typically decreases with decreasing separation for direct imaging surveys.

We have shown that the shape of the separation distribution is crucial for assessing the frequency of giant planets in surveys with many non-detections. However, the shape of the gas-giant planet distribution at orbital distances of a few times the snow line is poorly constrained. Some information is known about the M-star planet population in this range (e.g., Gould et al. 2010; Meyer et al. 2018), but the data suggest intrinsic differences between the M-star planet population and the population around more massive primaries, at least at semimajor axes that are well probed (e.g., Clanton & Gaudi 2014).

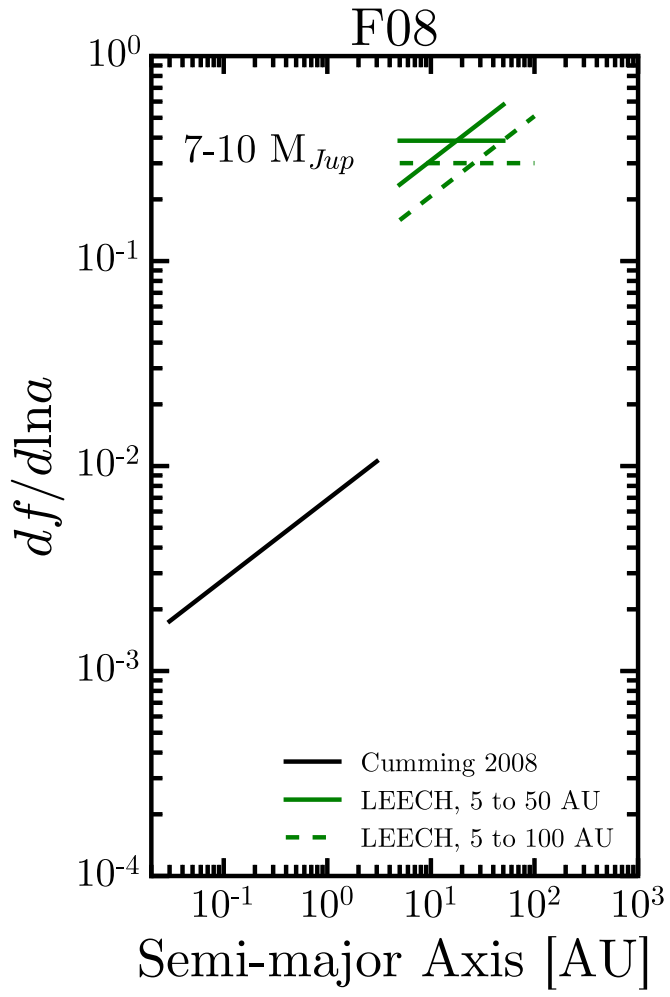

Figure 14. Same as for the plots in Figure 13 but specific to the cold-start models of Fortney et al. (2008).

To minimize the effects of needing to choose an underlying planet distribution in order to derive a planet occurrence frequency, the cautious approach is to use the measurement sensitivity within the region of interest to infer constraints on planet frequency for that range. In this context, the LEECH survey has added to our ability to constrain the gas-giant planet frequency on solar system scales by delivering sensitivity at smaller semimajor axes, a few snow-line radii from host stars (e.g., Figure 11).

7.2. Giant Planets and Transition Disks

Contrary to previous results, our analysis suggests that there is no discrepancy between the wide-gap ($\lesssim$90 au) transition disk frequency ($\gtrsim$11%; van der Marel et al. 2018) and the frequency of wide-orbit giant planets. For cold-start planets around solar-type stars, we know that if the shape of the RV planet population can be extrapolated to larger orbital separations, then it cannot extend beyond ~60 au (Brandt et al. 2014). However, if the RV planet distribution did extend to 60 au, this implies a frequency of 1–10 $M_{\rm Jup}$ planets on orbits from 5 to 60 au of 13.1%, consistent with the lower limit on the transition disk frequency. As we have discussed, it is unclear whether we should expect the giant-planet distribution to continue uniformly beyond the snow line in protoplanetary disks, so an actual constraint on the cold-start planet population from ~5 to 60 au is much more uncertain. The LEECH constraint is that $\lesssim$88% of FGK stars have a 7 to 10 $M_{\rm Jup}$ planet from 5 to 50 au, leaving open a wide range of possibilities, and we showed in Figure 11 that LEECH delivers some of the best cold-start constraints in this range. The tension reported by van der Marel et al. (2018) relied on hot-start constraints for the giant-planet occurrence frequency derived for a range of planet masses (5–13 $M_{\rm Jup}$) that does not extend low enough to capture all of the relevant gap-opening planets (Dodson-Robinson & Salyk 2011; Zhu et al. 2011).

So, while wide-orbit planets beyond the radii of typical protoplanetary disks are undoubtedly rare (e.g., Nielsen & Close 2010), and hot-start planets are somewhat rare even on solar system scales (e.g., Bowler 2016; Galicher et al. 2016), it is not necessary for gas-giant planets to be rare in the range of 5 to 100 au around solar mass primaries because they could be formed less than maximally luminous, and in this case direct imaging surveys are far less sensitive to detect them. Since the frequency of wide-orbit gas giants beyond the snow line is an important parameter for studying the formation and evolution of planetary systems, ongoing direct imaging surveys should include a measurement of their sensitivity to cold-start planets and calculate the corresponding occurrence frequencies or upper limits for orbital ranges $\lesssim$100 au.

Future observations with the *James Webb Space Telescope* (*JWST*) will also play an important role in probing for cold-start planets on solar system scales around nearby stars. Simulations using pyNRC[26] suggest that Near-Infrared Camera (NIRCam) will be background-limited beyond ~3″ when pairing the M430R coronagraphic mask with the F430M filter, reaching ~19th magnitude. Therefore, *JWST* will be capable of making background-limited probes interior to 100 au around stars within 30 pc. There are 70 FGK stars within 10 pc (Henry et al. 2018), scaling by volume there are nearly 2000 FGK stars within 30 pc.

The NIRCam F430M filter is similar to M', allowing us to make a direct comparison of the NIRCam background limit to the predictions for gas-giant planet brightness from evolutionary models. According to the COND evolutionary models, a 19th magnitude sensitivity limit should facilitate the detection of a 3 $M_{\rm Jup}$ planet at 10 pc, or a 6 $M_{\rm Jup}$ planet at 30 pc in a 5 Gyr system. The F444W filter will be employed more often than F430M for planet searches due to its broad wavelength coverage, providing an additional ~1 mag increase in overall sensitivity compared to F430M.

8. Conclusion

We presented the results of the LEECH direct imaging survey for wide-orbit gas-giant planets. LEECH was performed at 3.8 μm where colder planets emit more of their flux. This allowed us to emphasize proximity over youth in our target selection, resulting in increased sensitivity interior to 20 au compared to previous surveys.

We reached deeper average contrast around our targets than Rameau et al. (2013), who also reported the results of a large L' survey. We are typically $\gtrsim$1 mag more sensitive as a function of angular separation due to the performance of the LBT deformable secondary AO system and the thermal–infrared sensitivity of LBTI/LMIRcam. We are even more sensitive as a function of orbital radius in astronomical units after

[26] https://pynrc.readthedocs.io

accounting for the different average distance of our targets, 25 pc for LEECH and 40 pc for Rameau et al. (2013).

We converted our photometric limits to limits on the minimum detectable planet mass around each star by using evolutionary models to convert luminosity and age to mass. We used three different evolutionary models that bracket observations and span extreme assumptions regarding the zero-age–luminosity of planets and their atmospheric appearance.

Ages for each target were mostly taken from the literature. For our A- and B-type field stars, we derived ages following the approach of Nielsen et al. (2013). Our results are systematically older than those of Nielsen et al. (2013) for the stars in common, most likely because we use different model isochrones.

Our survey delivers the best-yet sensitivity to cold-start planets interior to 20 au around FGK stars. We used our survey results to place constraints on the wide-orbit giant-planet occurrence rate around these stars. We discussed how such limits depend sensitively on the choice of evolutionary model as well as the underlying planet distribution. We showed that when conservative choices are made (using cold-start evolutionary models and considering only a narrow range of semimajor axes not extending beyond the typical protoplanetary disk radius), the giant-planet occurrence frequency on 5–100 au orbits is not well constrained (Table 7). Planets in this range may be common.

J.M.S. is supported by NASA through Hubble Fellowship grant HST-HF2-51398.001-A awarded by the Space Telescope Science Institute, which is operated by the Association of Universities for Research in Astronomy, Inc., for NASA, under contract NAS5-26555. LEECH is funded by the NASA Origins of Solar Systems Program, grant NNX13AJ17G. K.M.M.'s work is supported by the NASA Exoplanets Research Program (XRP) by cooperative agreement NNX16AD44G. The results reported herein benefited from collaborations and/or information exchange within NASA's Nexus for Exoplanet System Science (NExSS) research coordination network at Arizona State University sponsored by NASAs Science Mission Directorate (grant NNX15AD53G). This material is based in part on work supported by the National Aeronautics and Space Administration under Agreement No. NNX15AD94G, Earths in Other Solar Systems, issued through the Science Mission Directorate interdivisional initiative Nexus for Exoplanet System Science. This research has made use of the Washington Double Star Catalog maintained at the U.S. Naval Observatory. This publication makes use of data products from the Two Micron All Sky Survey, which is a joint project of the University of Massachusetts and the Infrared Processing and Analysis Center/California Institute of Technology, funded by the National Aeronautics and Space Administration and the National Science Foundation. This work has made use of data from the European Space Agency (ESA) mission *Gaia* (https://www.cosmos.esa.int/gaia), processed by the *Gaia* Data Processing and Analysis Consortium (DPAC, https://www.cosmos.esa.int/web/gaia/dpac/consortium). Funding for the DPAC has been provided by national institutions, in particular the institutions participating in the *Gaia* Multilateral Agreement. This work benefited from the Exoplanet Summer Program in the Other Worlds Laboratory (OWL) at the University of California, Santa Cruz, a program funded by the Heising-Simons Foundation. The LBT is an international collaboration among institutions in the United States, Italy, and Germany. LBT Corporation partners are The University of Arizona on behalf of the Arizona university system; Istituto Nazionale di Astrofisica, Italy; LBT Beteiligungsgesellschaft, Germany, representing the Max-Planck Society, the Astrophysical Institute Potsdam, and Heidelberg University; The Ohio State University, and The Research Corporation, on behalf of The University of Notre Dame, University of Minnesota, and University of Virginia.

Appendix
Constructing More Modern Contrast Curves

We created contrast curves that account for small number statistics (e.g., Mawet et al. 2014) and provide a high level of completeness (e.g., Wahhaj et al. 2013). Our specific approach closely followed the example of Ruane et al. (2017), using a varying detection threshold with separation from the target star in order to provide a constant number of expected false detections at each radius (Jensen-Clem et al. 2018). Our curves are designed to deliver 95% completeness to objects above our threshold chosen to provide 0.01 total false detections per data set. In this appendix we discuss how we adjusted our classical 5σ contrast curves to meet these criteria.

For each target and for each radius, r, in units of λ/D, we define the acceptable number of false detections, $\langle N_{\rm false}(r)\rangle$, by dividing 0.01 total false detections per target evenly among the 28 annuli of λ/D width that exist in our 3″ field of view. We then solved for the corresponding acceptable false-positive fraction as a function of radius, FPF(r), using

$$\mathrm{FPF}(r) = \frac{\langle N_{\rm false}(r)\rangle}{2\pi r}, \tag{14}$$

where $2\pi r$ is the number of independent samples of the noise distribution at each radius. Thus, a larger false-positive fraction is used for smaller separations in our curves.

To connect our measured photometry S to false-positive fractions given an estimate of the noise level σ (derived using $n = 2\pi r$ independent samples of the noise), we use the value

$$t = \frac{S}{\sigma\sqrt{1 + 1/n}}, \tag{15}$$

which is t-distributed with $n - 1$ degrees of freedom, assuming the underlying noise distribution is intrinsically Gaussian (following, e.g., Ruane et al. 2017). We then calculated the necessary threshold for this value, $\tau(r)$, to attain our required FPF(r). To do this we used the percentage point function (or inverse cumulative distribution, ppf_t), of the t-distribution with $n - 1$ degrees of freedom,

$$\tau(r) = ppf_t(1 - \mathrm{FPF}(r), n - 1) + ppf_t(0.95, n - 1), \tag{16}$$

where the last term on the right is necessary to ensure 95% completeness.

Finally, we adjust our contrast curves to meet this threshold by adding

$$\Delta m_t(r) = 2.5\log_{10}\left(\frac{t_{\rm old}(r)}{\tau(r)}\right), \tag{17}$$

where $t_{\rm old}(r)$ is the t-value as a function of separation corresponding to our classical 5σ contrast curves,

$$t_{old}(r) = \frac{5}{\sqrt{1 + 1/n}}. \tag{18}$$

In Figure 15, we plot $\Delta m_t(r)$. The average adjustment to our classical contrast curves is 0.29 mag.

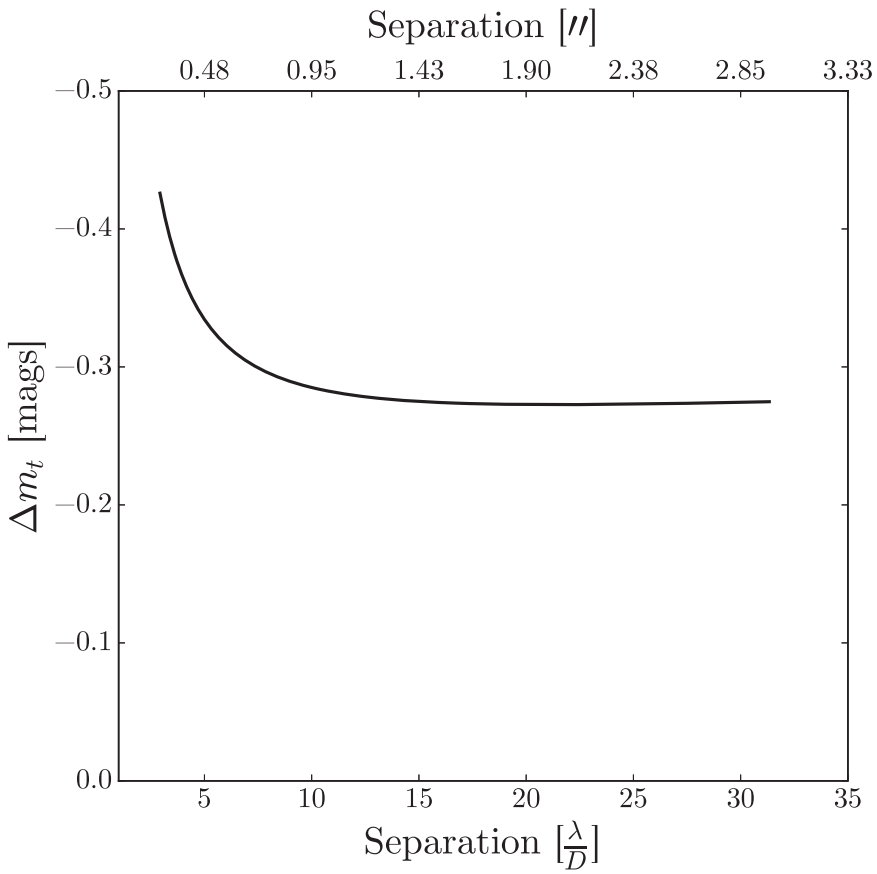

Figure 15. Contrast adjustment as a function of separation to convert our classical 5σ contrast curves to curves that indicate a constant number of expected false detections per radius, properly accounting for small number statistics, and ensuring 95% completeness.

ORCID iDs

Jordan M. Stone https://orcid.org/0000-0003-0454-3718
Andrew J. Skemer https://orcid.org/0000-0001-6098-3924
Mariangela Bonavita https://orcid.org/0000-0002-7520-8389
Kaitlin M. Kratter https://orcid.org/0000-0001-5253-1338
Anne-Lise Maire https://orcid.org/0000-0002-2591-4138
Vanessa P. Bailey https://orcid.org/0000-0002-5407-2806
Jarron M. Leisenring https://orcid.org/0000-0002-0834-6140
Beth Biller https://orcid.org/0000-0003-4614-7035
J. A. Eisner https://orcid.org/0000-0002-1031-4199
Justin R. Crepp https://orcid.org/0000-0003-0800-0593
Gerd Weigelt https://orcid.org/0000-0001-9754-2233
Joshua Schlieder https://orcid.org/0000-0001-5347-7062
Dániel Apai https://orcid.org/0000-0003-3714-5855
Kate Su https://orcid.org/0000-0002-3532-5580
Kimberly Ward-Duong https://orcid.org/0000-0002-4479-8291
Katie M. Morzinski https://orcid.org/0000-0002-1384-0063
Laird M. Close https://orcid.org/0000-0002-2167-8246
Jonathan J. Fortney https://orcid.org/0000-0002-9843-4354
Esther Buenzli https://orcid.org/0000-0003-3306-1486

References

Ammler-von Eiff, M., Bedalov, A., Kranhold, C., et al. 2016, A&A, 591, A84
Anderson, E., & Francis, C. 2012, AstL, 38, 331
Ansdell, M., Williams, J. P., Trapman, L., et al. 2018, ApJ, 859, 21
Bailey, V. P., Hinz, P. M., Puglisi, A. T., et al. 2014, Proc. SPIE, 9148, 914803
Baraffe, I., Chabrier, G., Allard, F., & Hauschildt, P. H. 2002, A&A, 382, 563
Baraffe, I., Chabrier, G., Barman, T. S., Allard, F., & Hauschildt, P. H. 2003, A&A, 402, 701
Baraffe, I., Homeier, D., Allard, F., & Chabrier, G. 2015, A&A, 577, A42
Barman, T. S., Konopacky, Q. M., Macintosh, B., & Marois, C. 2015, ApJ, 804, 61
Barman, T. S., Macintosh, B., Konopacky, Q. M., & Marois, C. 2011, ApJ, 733, 65
Batalha, N. M. 2014, PNAS, 111, 12647
Bell, C. P. M., Mamajek, E. E., & Naylor, T. 2015, MNRAS, 454, 593
Berardo, D., Cumming, A., & Marleau, G.-D. 2017, ApJ, 834, 149
Bessell, M. S., & Brett, J. M. 1988, PASP, 100, 1134
Biller, B. A., Liu, M. C., Wahhaj, Z., et al. 2013, ApJ, 777, 160
Bonavita, M., Chauvin, G., Desidera, S., et al. 2012, A&A, 537, A67
Bonavita, M., Desidera, S., Thalmann, C., et al. 2016, A&A, 593, A38
Bonnefoy, M., Zurlo, A., Baudino, J. L., et al. 2016, A&A, 587, A58
Bowler, B. P. 2016, PASP, 128, 102001
Bowler, B. P., Liu, M. C., Shkolnik, E. L., & Tamura, M. 2015, ApJS, 216, 7
Brandt, T. D., McElwain, M. W., Turner, E. L., et al. 2014, ApJ, 794, 159
Casagrande, L., Schönrich, R., Asplund, M., et al. 2011, A&A, 530, A138
Chabrier, G., Baraffe, I., Allard, F., & Hauschildt, P. 2000, ApJ, 542, 464
Chauvin, G., Lagrange, A.-M., Dumas, C., et al. 2005, A&A, 438, L25
Chauvin, G., Vigan, A., Bonnefoy, M., et al. 2015, A&A, 573, A127
Cignoni, M., Degl'Innocenti, S., Prada Moroni, P. G., & Shore, S. N. 2006, A&A, 459, 783
Clanton, C., & Gaudi, B. S. 2014, ApJ, 791, 91
Crepp, J. R., & Johnson, J. A. 2011, ApJ, 733, 126
Cumming, A., Butler, R. P., Marcy, G. W., et al. 2008, PASP, 120, 531
Currie, T., Burrows, A., Itoh, Y., et al. 2011, ApJ, 729, 128
Cutri, R. M., Skrutskie, M. F., van Dyk, S., et al. 2003, in 2MASS All Sky Catalog of Point Sources, 0
Delorme, P., Lagrange, A. M., Chauvin, G., et al. 2012, A&A, 539, A72
Dodson-Robinson, S. E., & Salyk, C. 2011, ApJ, 738, 131
Duchêne, G., & Kraus, A. 2013, ARA&A, 51, 269
Eggen, O. J. 1991, AJ, 102, 2028
Eisner, J. A., Arce, H. G., Ballering, N. P., et al. 2018, ApJ, 860, 77
Filippazzo, J. C., Rice, E. L., Faherty, J., et al. 2015, ApJ, 810, 158

Fortney, J. J., Marley, M. S., Saumon, D., & Lodders, K. 2008, ApJ, 683, 1104
Gagné, J., Mamajek, E. E., Malo, L., et al. 2018, ApJ, 856, 23
Gaia Collaboration, Brown, A. G. A., Vallenari, A., et al. 2018, arXiv:1804.09365
Galicher, R., Marois, C., Macintosh, B., et al. 2016, A&A, 594, A63
Gáspár, A., Rieke, G. H., & Balog, Z. 2013, ApJ, 768, 25
Gould, A., Dong, S., Gaudi, B. S., et al. 2010, ApJ, 720, 1073
Hayashi, C. 1981, PThPS, 70, 35
Heinze, A. N., Hinz, P. M., Kenworthy, M., et al. 2010a, ApJ, 714, 1570
Heinze, A. N., Hinz, P. M., Sivanandam, S., et al. 2010b, ApJ, 714, 1551
Henry, T. J., Jao, W.-C., Winters, J. G., et al. 2018, AJ, 155, 265
Hinz, P. M., Defrère, D., Skemer, A., et al. 2016, Proc. SPIE, 9907, 990704
Hinz, P. M., Rodigas, T. J., Kenworthy, M. A., et al. 2010, ApJ, 716, 417
Holman, M. J., & Wiegert, P. A. 1999, AJ, 117, 621
Hubeny, I., & Burrows, A. 2007, ApJ, 669, 1248
Hubickyj, O., Bodenheimer, P., & Lissauer, J. J. 2005, Icar, 179, 415
Ingraham, P., Marley, M. S., Saumon, D., et al. 2014, ApJL, 794, L15
Jensen-Clem, R., Mawet, D., Gomez Gonzalez, C. A., et al. 2018, AJ, 155, 19
Jones, J., White, R. J., Boyajian, T., et al. 2015, ApJ, 813, 58
Kasper, M., Apai, D., Janson, M., & Brandner, W. 2007, A&A, 472, 321
King, J. R., Villarreal, A. R., Soderblom, D. R., Gulliver, A. F., & Adelman, S. J. 2003, AJ, 125, 1980
Konopacky, Q. M., Barman, T. S., Macintosh, B. A., & Marois, C. 2013, Sci, 339, 1398
Lafrenière, D., Doyon, R., Marois, C., et al. 2007a, ApJ, 670, 1367
Lafrenière, D., Marois, C., Doyon, R., Nadeau, D., & Artigau, É. 2007b, ApJ, 660, 770
Lambrechts, M., & Johansen, A. 2012, A&A, 544, A32
Lannier, J., Delorme, P., Lagrange, A. M., et al. 2016, A&A, 596, A83
Leisenring, J. M., Skrutskie, M. F., Hinz, P. M., et al. 2012, Proc. SPIE, 8446, 84464F
Liu, M. C., Dupuy, T. J., & Allers, K. N. 2016, ApJ, 833, 96
Liu, M. C., Wahhaj, Z., Biller, B. A., et al. 2010, Proc. SPIE, 7736, 77361K
Macintosh, B., Graham, J. R., Barman, T., et al. 2015, Sci, 350, 64
Maire, A.-L., Skemer, A. J., Hinz, P. M., et al. 2015, A&A, 579, C2
Mamajek, E. E., & Hillenbrand, L. A. 2008, ApJ, 687, 1264
Marigo, P., Girardi, L., Bressan, A., et al. 2017, ApJ, 835, 77
Marley, M. S., Fortney, J. J., Hubickyj, O., Bodenheimer, P., & Lissauer, J. J. 2007, ApJ, 655, 541
Marley, M. S., Saumon, D., Cushing, M., et al. 2012, ApJ, 754, 135
Marois, C., Lafrenière, D., Doyon, R., Macintosh, B., & Nadeau, D. 2006, ApJ, 641, 556
Mawet, D., Milli, J., Wahhaj, Z., et al. 2014, ApJ, 792, 97
Meshkat, T., Kenworthy, M. A., Reggiani, M., et al. 2015, MNRAS, 453, 2533
Meshkat, T., Mawet, D., Bryan, M. L., et al. 2017, AJ, 154, 245
Meyer, M. R., Amara, A., Reggiani, M., & Quanz, S. P. 2018, A&A, 612, L3
Mordasini, C. 2013, A&A, 558, A113
Mordasini, C., Marleau, G.-D., & Mollière, P. 2017, A&A, 608, A72
Nielsen, E. L., & Close, L. M. 2010, ApJ, 717, 878
Nielsen, E. L., Liu, M. C., Wahhaj, Z., et al. 2013, ApJ, 776, 4
Nieva, M.-F., & Przybilla, N. 2012, A&A, 539, A143
Ormel, C. W., & Klahr, H. H. 2010, A&A, 520, A43
Press, W. H., Teukolsky, S. A., Vetterling, W. T., & Flannery, B. P. 2002, in Numerical Recipes in C++: the Art of Scientific Computing, 1002
Rajan, A., Rameau, J., De Rosa, R. J., et al. 2017, AJ, 154, 10
Rameau, J., Chauvin, G., Lagrange, A.-M., et al. 2013, A&A, 553, A60
Reggiani, M., Meyer, M. R., Chauvin, G., et al. 2016, A&A, 586, A147
Rieke, G. H., Su, K. Y. L., Stansberry, J. A., et al. 2005, ApJ, 620, 1010
Ruane, G., Mawet, D., Kastner, J., et al. 2017, AJ, 154, 73
Sallum, S., Follette, K. B., Eisner, J. A., et al. 2015, Natur, 527, 342
Salpeter, E. E. 1955, ApJ, 121, 161
Samland, M., Mollière, P., Bonnefoy, M., et al. 2017, A&A, 603, A57
Schlieder, J. E., Skemer, A. J., Maire, A.-L., et al. 2016, ApJ, 818, 1
Siess, L., Dufour, E., & Forestini, M. 2000, A&A, 358, 593
Skemer, A. J., Close, L. M., Szűcs, L., et al. 2011, ApJ, 732, 107
Skemer, A. J., Hinz, P., Esposito, S., et al. 2014a, Proc. SPIE, 9148, 91480L
Skemer, A. J., Hinz, P. M., Esposito, S., et al. 2012, ApJ, 753, 14
Skemer, A. J., Marley, M. S., Hinz, P. M., et al. 2014b, ApJ, 792, 17
Skemer, A. J., Morley, C. V., Zimmerman, N. T., et al. 2016, ApJ, 817, 166
Skrutskie, M. F., Cutri, R. M., Stiening, R., et al. 2006, AJ, 131, 1163
Skrutskie, M. F., Jones, T., Hinz, P., et al. 2010, Proc. SPIE, 7735, 77353H
Soummer, R., Pueyo, L., & Larkin, J. 2012, ApJL, 755, L28
Tamura, M. 2016, PJAB, 92, 45
Tazzari, M., Testi, L., Natta, A., et al. 2017, A&A, 606, A88
Thorngren, D. P., Fortney, J. J., Murray-Clay, R. A., & Lopez, E. D. 2016, ApJ, 831, 64
van der Marel, N., Williams, J. P., Ansdell, M., et al. 2018, ApJ, 854, 177
Wagner, K., Follette, K. B., Close, L. M., et al. 2018, arXiv:1807.10766
Wahhaj, Z., Liu, M. C., Biller, B. A., et al. 2013, ApJ, 779, 80
Wong, M. H., Mahaffy, P. R., Atreya, S. K., Niemann, H. B., & Owen, T. C. 2004, Icar, 171, 153
Zhu, Z., Nelson, R. P., Hartmann, L., Espaillat, C., & Calvet, N. 2011, ApJ, 729, 47
Zuckerman, B., Rhee, J. H., Song, I., & Bessell, M. S. 2011, ApJ, 732, 61